

Chemical composition of intermediate mass stars members of the M6 (NGC 6405) open cluster

T. Kılıçoğlu

Ankara University, Faculty of Science, Department of Astronomy and Space Sciences,
06100, Tandoğan, Ankara, Turkey

tkilicoglu@ankara.edu.tr

R. Monier¹

LESIA, UMR 8109, Observatoire de Paris Meudon, Place J. Janssen, Meudon, France

Richard.Monier@obspm.fr

J. Richer

Département de physique, Université de Montréal, 2900, Boulevard Edouard-Montpetit,
Montréal QC, Canada H3C 3J7

Jacques.Richer@umontreal.ca

L. Fossati

Argelander-Institut für Astronomie der Universität Bonn, Auf dem Hügel 71, 53121, Bonn,
Germany

lfossati@astro.uni-bonn.de

and

B. Albayrak

Ankara University, Faculty of Science, Department of Astronomy and Space Sciences,
06100, Tandoğan, Ankara, Turkey

balbayrak@ankara.edu.tr

Received _____; accepted _____

to appear in Astronomical Journal

¹Laboratoire Lagrange UMR 7293, Université de Nice Sophia, Nice, France

ABSTRACT

We present here the first abundance analysis of 44 late B, A and F-type members of the young open cluster M6 (NGC 6405, age about 75 Myrs). Low and medium resolution spectra, covering the 4500 to 5800 Å wavelength range, were obtained using the FLAMES/GIRAFFE spectrograph attached to the ESO Very Large Telescopes (VLT). We determined the atmospheric parameters using calibrations of the Geneva photometry and by adjusting the H_β profiles to synthetic ones. The abundances of up to 20 chemical elements, from helium to mercury, were derived for 19 late B, 16 A and 9 F stars by iteratively adjusting synthetic spectra to the observations. We also derived a mean cluster metallicity of $[\text{Fe}/\text{H}] = 0.07 \pm 0.03$ dex from the iron abundances of the F-type stars. We find that, for most chemical elements, the normal late B and A-type stars exhibit larger star-to-star abundance variations than the F-type stars do probably because of the faster rotation of the B and A stars. The abundances of C, O, Mg, Si and Sc appear to be anticorrelated to that of Fe, while the opposite holds for the abundances of Ca, Ti, Cr, Mn, Ni, Y, and Ba about as expected if radiative diffusion is efficient in the envelopes of these stars. In the course of this analysis, we discovered five new peculiar stars: one mild-Am, one Am, and one Fm star (HD 318091, CD-32 13109, GSC 07380-01211), one HgMn star (HD 318126), and one He-weak P-rich (HD 318101) star. We also discovered a new spectroscopic binary, most likely a SB2. We performed a detailed modelling of HD 318101, the new He-weak P-rich CP star, using the Montréal stellar evolution code XEVOL which treats self-consistently all particle transport processes. Although the overall abundance pattern of this star is properly reproduced, we find that detailed abundances (in particular the high P excess) resisted modelling attempts even when a range of turbulence profiles and mass loss rates were considered. Solutions

are proposed, which are still under investigation.

Subject headings: stars: abundances — open clusters: individual(M6) —stars
individual: HD 318101

1. Introduction

Abundance determinations of late-B, A and F dwarfs in open clusters aim at elucidating the mechanisms of mixing at play in the interiors of these main-sequence stars. Indeed open clusters are excellent laboratories to test stellar evolution as the stars members of an open cluster originate from the same original interstellar material and have the same initial chemical composition and age.

This paper follows two series of paper addressing the chemical composition of F, A and late B-type dwarfs in open clusters and/or moving groups of different ages: i) Varenne & Monier (1999), Monier (2005), Gebran & Monier (2008), Gebran et al. (2008), and Gebran et al. (2010) for the Hyades, the Ursa Major Moving Group, Coma Berenices, and the Pleiades, ii) Fossati et al. (2007), Fossati et al. (2008), and Fossati et al. (2011) for Praesepe and NGC 5460. A review can be found in Fossati (2014).

The main objective of these works is twofold: first, we wish to improve our knowledge of the chemical composition of late-B, A and F dwarfs, and second, we aim at using these determinations to set constraints on particle transport processes in self consistent evolutionary models. Other groups also performed abundance analysis of intermediate-mass stars in open clusters, with a variety of goals (Stütz et al. 2006; Villanova et al. 2009; Pace et al. 2010; Pancino et al. 2010; Jacobson et al. 2011; Carrera & Pancino 2011; Carraro et al. 2014).

In this paper, we present the first abundance analysis of 44 late B, A and F-type dwarfs members of the young open cluster M6. M6 (NGC 6405) is an interarm object lying between the local arm and the Sagittarius arm (Vleeming 1974). It is a moderately-rich cluster (van den Bergh & Hagen 1975) and it contains about 120 most-likely members (for $V \leq 15.1$) according to Antalová (1972). Previous age, distance, color excess and metallicity determinations for the cluster are collected in Table 1, along with our determinations

(see Sec. 4.1.2 and 2.1). Early estimates of the distance, reddening and age of the cluster were obtained photometrically by Rohlfs et al. (1959)¹ who derived a distance of 630 pc from photoelectric UBV observations of 132 stars, a mean reddening $E(B-V)$ of 0.156 mag and estimated an age of 100 Myr. In a similar manner, Eggen (1960) derived a distance of 505 pc from photometric observations of 66 stars and a mean reddening $E(B-V)=0.13$ mag. After a careful removal of field stars, Vleeming (1974) has derived a colour excess $E(B-V)=0.15$ mag, a distance of 450 pc and an age of about 100 Myr. Schneider (1985) performed Strömgren photometry of M6 up to $V=12.0$ mag, and derived a reddening of $E(b-y) = 0.110$. Maitzen & Schneider (1984) reported the detection of 3 chemically peculiar stars, with star number 77 exhibiting one of the strongest 5200 Å depression ever measured. Cameron (1985a) used the extinction corrected ultraviolet excess of stars in a color-color diagram to estimate the average metallicity, obtaining $[Fe/H] \sim 0.07$ dex.

In this work, we have derived the abundances of up to 20 chemical elements, from Helium to Mercury, for 19 B, 16 A and 9 F-type stars observed with the GIRAFFE spectrograph in the wavelength range from 4500 up to 5840 Å. The spectral types of these stars range from B5 (i.e. a mass of about $4.3 M_{\odot}$) to F6 ($1.4 M_{\odot}$). We have looked for star-to-star variations of the elemental abundances, in particular for the B and A-type stars, and searched for putative correlations of the various abundances with effective temperature, projected rotational velocity and the iron abundance. In the framework of radiative diffusion, the abundances of a few elements, in particular manganese, are expected to increase with effective temperature and should remain insensitive to rotation up to 120 km s^{-1} since the timescale of diffusion are much shorter than those of rotational mixing (Charbonneau & Michaud 1991). In the course of this abundance analysis, we have

¹In this study, we use the identification number of the stars in the region of M6 from Rohlfs et al. (1959).

discovered five new chemically peculiar stars and a double-lined spectroscopic binary.

The target selection, membership assessment, and data reduction are described in section 2. The determination of the effective temperatures and surface gravities (T_{eff} and $\log g$), and abundance analysis are discussed in section 3. We discuss our results in Sections 4 and 5. In section 5, we provide a detailed modeling of HD 318101, one of the newly found CP star, using the Montréal stellar evolution code XEVOL. Conclusions are gathered in Section 6.

2. Observations, Data Reduction and Target Selection

The spectra of 104 objects in the region of M6 were obtained using the Fibre Large Array Multi Element Spectrograph (FLAMES) instrument with the GIRAFFE spectrograph attached to the Unit 2 Kueyen of the Very Large Telescopes (VLT) at the European Southern Observatory (ESO) by one of us (LF). The instrument settings and target selection were carried out in the same way as described by Fossati et al. (2011).

Three different gratings were chosen for GIRAFFE: LR3, HR09B, and HR11. The low resolution ($R=\lambda/\Delta\lambda=7500$) LR3 setting, covering the 4490–5080 Å wavelength range, includes the H_β line and several strong lines of neutrals and singly ionized elements. The wide wavelength range of these single-order spectra encompasses the entire H_β line with at least 200 Å extension on each side of the H_β line, allowing a proper continuum normalisation of the Balmer line. The two medium resolution ($R\sim 25000$) HR09B and HR11 settings, covering respectively the 5140–5380 and 5450–5750 Å wavelength ranges, were also adopted to derive abundances of further elements and with higher accuracy. In addition, the higher resolution spectra allow for a more precise determination of the projected rotational velocity ($v_e \sin i$).

The spectra were reduced using the standard GIRAFFE data processing pipeline, which includes scattered light correction². In order to correct for the sky background, we averaged the 4–6 sky spectra which have been obtained closest to each star, and subtracted the average sky spectrum from each corresponding stellar spectrum. Each star was observed twice, six times, and three times with the LR3, HR09B, and HR11 settings, respectively, on May 30th and June 5th, 2007. We co-added the spectra obtained with the same gratings in order to increase the signal-to-noise ratio (S/N), after correcting for the barycentric velocity correction. Using the spectra obtained with the HR09B setting, we looked for radial velocity variations (which were measured using cross-correlation with appropriate synthetic spectra). In the event we found significant radial velocity variations, we shifted the spectra to the same reference frame before co-addition. The observing log is given in Table 2.

The spectra were normalized to selected continuum points, ie. regions we knew free of lines from our synthetic spectra calculations, adjusting a smooth spline function through these points. In the event that no true continuum could be found (e.g., for rapidly rotating stars or for the cooler stars), pseudo-continuum windows were selected and the location of the true continuum retrieved using synthetic spectra convolved for the appropriate rotation rate. All the spectra acquired with the HR11 setting show broad absorption features, much wider than the neighbouring stellar absorption lines. These broad features are located at 5705.65 Å, 5780.54 Å, and 5797.16 Å and correspond to three well-known diffuse interstellar bands (DIBs).

Since most members of the M6 open cluster still lack a radial velocity determination, their membership has yet to be firmly established. In order to select the most-likely cluster members, we first estimated effective temperatures, projected rotational velocities, and radial velocities by performing a preliminary spectral analysis, in a similar way as

²[http : //www.eso.org/observing/dfo/quality/GIRAFFE/pipeline/pipe_reduc.html](http://www.eso.org/observing/dfo/quality/GIRAFFE/pipeline/pipe_reduc.html)

described in Sect. 3. We primarily considered 56 targets with $T_{\text{eff}} > 6100 \text{ K}$ and spectra with $S/N \sim 100$, and selected 44 targets to perform a more thorough spectral analysis considering the membership from three criteria: i) proper motions, ii) radial velocity, and iii) position of the stars in the Hertzsprung-Russell (HR) diagram (Table 3).

According to Frinchaboy & Majewski (2008), only six stars (nos. 1 [BM Sco], 17, 20, 72, 77 [V970 Sco], and HD 318111) have been identified as cluster members from proper motions and radial velocity, with an averaged radial velocity of $-8.27 \pm 0.45 \text{ km s}^{-1}$. As a first criterion, we considered the stars for which we derived a radial velocity which differs by more than $\pm 5 \text{ km s}^{-1}$ from this average value as non-members. We then checked the membership probability of the remaining stars against Dias et al. (2006) and Frinchaboy & Majewski (2008), who derived membership probabilities for stars in the field of view of M6 using high precision proper motions from the UCAC catalogue (Zacharias et al. 2004) and the Tycho-2 catalogue, respectively. As a second criterion, we adopted as members the remaining stars having a membership probability larger than 25% according to either Dias et al. (2006) or Frinchaboy & Majewski (2008). We finally checked the locations of the remaining stars in the HR diagram (see Sec. 2.1 for details). The stars which were found to lie on the average age isochrone were considered as members. Applying these three criteria yields a final list of 44 certain members (ie. with a membership probability of 100 %).

We have searched various sources for possible binarity of the 44 retained members. According to the photometric studies of M6 by Antalová (1972), Maitzen & Schneider (1984), and Schneider (1985), none of the 44 retained stars is known to be a binary . Inspection of the CCDM catalogue (Dommanget & Nys 1995) reveals that HD 160167 (no. 115) is a double star. The difference in radial velocity between our measurements and those of Frinchaboy & Majewski (2008) supports the binary nature of HD 160167. However, we could not find any evidence of the lines of the secondary in our spectra. This star may

be a SB1 and we analysed it as a single star.

2.1. The Hertzsprung-Russell diagram of the cluster

The Hertzsprung-Russell (HR) diagram of M6 is shown on Fig. 1 displaying luminosities versus against the effective temperatures determined in section 3.2.1. We retrieved the Johnson UB_V photometry of the stars from the WEBDA database. The luminosities were derived from the V magnitudes and the bolometric corrections from Bessell et al. (1998), and an atmospheric extinction ($A_V = 0.47 \pm 0.06$) calculated from :

$$A_V = 3.14E(B - V) \quad (\text{Schultz \& Wiemer 1975}).$$

We adopted a color excess $E(B - V)$ of 0.15 ± 0.01 (see Table 1). The uncertainties of the distance of the cluster (± 50 pc), the first coefficient in the formula of Schultz & Wiemer (1975, ± 0.10), and the color excess (± 0.01) yield a typical uncertainty on $\log \frac{L}{L_\odot}$ of about ± 0.14 . The luminosities are derived from the total integrated flux (estimated from the V magnitudes corrected with the bolometric corrections) and the distance d by: $L = 4\pi d^2 F$.

In the HR diagram of Fig. 1, the normal B, A and F-type stars are depicted as filled circle. Special symbols depict the five chemically peculiar stars and one double-lined SB. which we have discovered in the course of this analysis. We have not corrected the luminosities of binaries since we did not know the contribution of the secondary to the total flux.

We estimated the distance and age of the M6 cluster by adjusting isochrones retrieved from the PARSEC³ library (Bressan et al. 2012). This site allows to compute isochrones

³<http://stev.oapd.inaf.it/cgi-bin/cmd>

specifically for the found cluster metallicity, which is $Z_{\text{cluster}} = 1.175Z_{\odot}$ (see sec. 4.1.2) for M6. We thus derived a distance of 400 ± 50 pc and an age of 75 ± 25 Myr for M6. We have collected the luminosities, masses, and fractional ages of the members of M6 (following Landstreet et al., 2007) in Table 4.

3. Abundance analysis

3.1. Model atmospheres, spectrum synthesis and atomic data

Model atmospheres were computed for the fundamental parameters of each star assuming solar composition (Grevesse & Sauval 1998) using the Linux version of the ATLAS9 code (Kurucz 1993; Sbordone et al. 2004; Sbordone 2005). These models assume a plane-parallel geometry, Hydrostatic Equilibrium (HE), Radiative Equilibrium (RE), and Local Thermodynamical Equilibrium (LTE). We used the new opacity distribution function (ODF) tables described in Castelli & Kurucz (2003). For stars cooler than 8500 K, convection was included adopting a mixing length parameter (α) of 0.5 for $7000 \text{ K} \leq T_{\text{eff}} \leq 8500 \text{ K}$, and 1.25 for $T_{\text{eff}} < 7000 \text{ K}$ according to the prescriptions in Smalley (2004). Each model has 72 layers and was converged up to $\log \tau = -6.875$ usually within 15 iterations. For the five stars we identified as new Chemically Peculiar stars, we have computed ATLAS12 model atmospheres for the first set of peculiar abundances found with ATLAS9. New abundances were derived by adjusting synthetic spectra to the observed ones and the process was iterated until the abundances derived from spectral synthesis and those included in ATLAS12 were the same. Convergence was in generally met in two iterations. The temperature profile $T(\tau_{5000})$ in these ATLAS12 models differs little from the ATLAS9 models as the elements whose abundances were adjusted are not very abundant elements.

Abundances were derived by adjusting grids of synthetic spectra convolved with the

appropriate rotation and instrumental profile to the normalized observed spectra since several of the retained stars rotate fairly fast and we deal with two different resolutions. The synthetic spectra were calculated using SYNSPEC48 (Hubeny & Lanz 1995) and its SYNLOT interface. We adopted the solar abundances from Grevesse & Sauval (1998). We used Procyon (F5V) (Griffin & Griffin 1979) , whose fundamental parameters are accurately known and whose composition is about solar (Steffen 1985), as a control star for the spectrum synthesis. While attempting to synthesize the observed Sc II lines of Procyon, we realized that SYNSPEC48 produces systematically too strong Sc II lines. Frémat et al. (2005) already reported on this problem for a previous version of SYNSPEC. As Frémat et al. (2005) did, we incorporated the PFSHA routine of ATLAS9 relative to Scandium into SYNSPEC48 and used this modified code (hereafter referred to as SYNSPEC48mod). The synthetic spectra were broadened by a gaussian profile corresponding to the appropriate instrument resolving power and by a parabolic profile for the appropriate $v_e \sin i$ of the star using the routine ROTIN3 provided along with SYNSPEC48 (this follows equation 18.14 in Gray (2005)) We modified the IDL graphic interface SYNLOT and implemented a routine which searches for the minimum of the χ^2 between the synthetic spectrum and the observed spectrum within a wavelength range specified by the user.

We created an atomic linelist by using first the file GFALL.DAT from Kurucz’s database⁴, restricted to the 4490–5850 Å wavelength interval. This list includes line data mostly from the literature for the light and the heavy elements with critically evaluated transition probabilities of Martin et al. (1988) and Fuhr et al. (1988) and computed data by Kurucz (1992) for the iron group elements. In the event more recent and more accurate atomic data were available, we updated all oscillator strengths using the VALD3 database

⁴<http://kurucz.harvard.edu/linelists.html>

(Piskunov et al. 1995; Ryabchikova et al. 1997; Kupka et al. 1999, 2000). VALD3 includes the critically evaluated transition probabilities of P II (Miller et al. 1971; Hibbert 1988), Ca II (Theodosiou 1989), Sc II (Lawler & Dakin 1989), Ti II (Pickering et al. 2002), Cr II (Bergeson & Lawler 1993; Sigut & Landstreet 1990; Pinnington et al. 1993), Fe II (Raassen & Uylings 1998), Ni I (Wickliffe & Lawler 1997), and Zr II (Cowley & Corliss 1983; Ljung et al. 2006). For the elements having more recent measurements of their oscillator strengths, we resorted to specific publications using the NIST Atomic Spectra Database (Kramida et al. 2013): He I (Wiese & Fuhr 2009), C and O (Wiese et al. 1996), Mg II (Kelleher & Podobedova 2008b), Si II (Kelleher & Podobedova 2008a), S II (Podobedova et al. 2009), Fe I (Fuhr & Wiese 2006; O’Brian et al. 1991), Y II (Fuhr & Wiese 2005), and Ba II (Curry 2004). The final linelist contains 90 944 lines in the range 4490–5850 Å. The lines actually used for the abundance determinations, are collected in Table 6 with their atomic data and sources. Most of the lines modeled here are weak lines formed deep in the atmospheres where LTE should prevail. They are well-suited to abundance determinations.

Although we do not expect to detect broadening due to hyperfine structure at the resolution of the GIRAFFE spectra, we did introduce hyperfine components for a few lines of Mn I and Sc II using the atomic data for each hyperfine transition from GFHYPERALL.DAT (Kurucz 1993) in order to derive more realistic abundances for these two elements.

All damping constants were initially taken from GFALL.DAT and then updated, in the event more recent and accurate values were available from VALD3. For a few Si II lines, we took the damping constants from Lanz et al. (1988). When they are set to zeros in the linelist, the damping constants are computed in SYNSPEC48mod using the approximation given by Kurucz & Avrett (1981). The broadening of the He I lines in SYNSPEC48mod uses specific tables, either from Shamey (1969) or Dimitrijevic & Sahal-Brechot (1984).

The broadening of the H I lines uses the tables of Vidal et al. (1973).

3.2. Determination of the atmospheric parameters

3.2.1. *Effective temperatures and surface gravities*

We first estimated the effective temperature and surface gravity for each star using the Geneva 7 color photometry retrieved from the WEBDA database⁵ and the CALIB code (North, P., private communication), based on the calibrations of Kunzli et al. (1997). Indeed, we could not use Napiwotzki et al. (1993)’s UVBYBETA routine since the 44 selected targets do not have Strömgren’s photometry. To derive T_{eff} and $\log g$, we used the CALIB code which calibrates pairs of Geneva photometric indexes (X, Y) , (pG, pT) , and $(d, B_2 - V_1)$ in terms of effective temperature and surface gravity respectively for hot, intermediate, and cool stars. We used the calibration of (X, Y) for the late B stars, (pG, pT) for the A stars and early F stars, and $(d, B_2 - V_1)$ for the late F stars. We corrected the $B_2 - V_1$ indexes affected by reddening, by a color excess correction $E(B_2 - V_1)$. As Maitzen & Schneider (1984) reported that there is no differential reddening across the area covered by M6, we corrected $B_2 - V_1$ with the average color excess $E(B_2 - V_1) = 0.13 \pm 0.01$ adopted from the literature (see Table 1). In order to convert $E(B - V)$ or $E(b - y)$ into a Geneva color excess $E(B_2 - V_1)$, we used the following two relations given by Crawford (1978) and Nicolet (1981), respectively:

$$E(b - y) = 0.74E(B - V),$$

$$E(B_2 - V_1) = 0.84E(B - V).$$

We then checked these first estimates of the effective temperatures and surface gravities

⁵<http://www.univie.ac.at/webda/navigation.html>

i) by adjusting synthetic spectra to the observed H_β line and ii) by studying the ionization equilibrium of Fe I and Fe II. Fig. 2 shows the comparison between the observed and best fitting synthetic H_β line profiles for 10 stars sorted out according to decreasing effective temperature from top to bottom. For stars with $T_{\text{eff}} \geq 8500$ K, the H_β line depends on both T_{eff} and $\log g$. For this reason we also used the ionisation equilibrium of Fe (I–II) to additionally constrain $\log g$ only for the slow rotators with $v_e \sin i \leq 80 \text{ km s}^{-1}$. We first derived the iron abundance from all unblended Fe I and Fe II lines. We then determined the set of $T_{\text{eff}} - \log g$ parameters which verified the ionisation equilibrium (ie. T_{eff} and $\log g$ were altered until the iron abundance derived from the Fe I lines be equal to that derived from the Fe II lines). We then finally checked that the found parameters did provide a good fit to the H_β line profile. When applying the ionisation equilibrium, we considered that Fe I lines may be affected by non-LTE effects, which would lead to a slight underestimation of the Fe abundance (e.g., Mashonkina et al. (2011)). For stars with $T_{\text{eff}} \leq 8500$ K, the H_β line profile is sensitive primarily to variations in T_{eff} and provides reliable effective temperatures. In the event the surface gravity for these cooler stars could not be derived from the ionisation equilibrium, we adopted the photometric $\log g$ value. The adopted atmospheric parameters of the analysed stars are collected in Table 5.

3.2.2. Projected apparent rotational velocities

The projected rotational velocities were obtained by adjusting the observed weak and moderately strong Fe II lines with synthetic spectra convolved with different rotational velocities (Fig 3, left panel). For faster rotating stars, with $v_e \sin i \geq 80 \text{ km s}^{-1}$, we estimated the $v_e \sin i$ value by fitting the profile of a few blended strong Fe II lines (Fig 3, right panel). The iron abundance was also adjusted if necessary. The final $v_e \sin i$ values were adopted by averaging the derived $v_e \sin i$ values from individual lines for each star.

3.2.3. Microturbulent velocities

To derive the microturbulent velocities, we followed the method described by Fossati et al. (2007) which consists in minimizing the standard deviation of the iron abundance derived from each individual Fe II line (Fig. 4). In the event the number of Fe II lines was not sufficient to apply this method (for the hottest stars), the microturbulent velocity was left as free parameter in the fitting iterations performed to derive the iron abundance (see Sect. 3.3). We checked whether there is a difference in the derived v_{mic} using these two approaches, applying both methods to slow rotators. We found that the second approach (v_{mic} as a free parameter) typically gives only about 0.1-0.2 km/s larger v_{mic} values⁶. That minor difference was taken into account in the uncertainty analysis. For the fastest rotating B-type stars, very few absorption lines are available to constrain the microturbulent velocity; for this reason we adopted a null microturbulent velocity (i.e., 0.0 km s⁻¹) with an assumed uncertainty of 1.0 km s⁻¹, which is a value commonly reported for main sequence late B-type stars by Fitzpatrick & Massa (1999). Only for one very slowly rotating chemically peculiar B-type star (HD 318126) could we derive the microturbulent velocity, obtaining 0.5 km s⁻¹.

3.3. Abundance determinations and their systematic errors

Since the rotational velocities of the analyzed stars range from 5.1 km s⁻¹ up to 310 km s⁻¹, the lines can be significantly broadened by rotation. We therefore used spectral

⁶This difference mostly stems from the different line selection between the two approaches. The method of Fossati et al. (2007) takes into account the unblended lines of selected singly-ionized element/elements only, while the other includes all lines of each element present in the spectrum.

synthesis to derive the elemental abundances. The abundances, expressed relatively to the solar ones⁷ ((Grevesse & Sauval 1998)) , of twenty elements were obtained by iteratively adjusting synthetic spectra to the normalised observed spectra and by performing a χ^2 minimization fit on the selected lines. For a given chemical element, the final abundance $[\frac{X}{H}]$ is an average of the abundances derived from each transition (i):

$$\langle [\frac{X}{H}] \rangle = \frac{\sum_i [\frac{X}{H}]_i}{N}$$

where N is the number of transitions for the element and $[\frac{X}{H}]_i$ the abundance derived for transition (i).

For each star, the final absolute abundances (expressed as $\text{Log}(X/H)$) are collected in table 7. As M6 is a young open cluster, we have also expressed in table 8 our abundances with respect to the cosmic abundances derived for young early B stars by Nieva & Przybilla (2012). We expect the abundances of the following elements: Fe, Ti, Cr Mg, Mn, C, Ca and Ni to be fairly reliable as we synthesized several lines of quality A to D for these elements. For the hottest stars, between B8 and A5, the oxygen abundance was derived mainly from the O I triplet near 5330 Å. For Y, several lines are available but their uncertainties are unknown so $[Y/H]$ should be taken with caution.

In order to evaluate the systematic errors on the derived mean abundances, we reanalyzed a few representative B-, A-, and F-type stars (nos. 17, 20, 47, 66, 99) by slightly altering the T_{eff} , $\log g$, v_{mic} , and the continuum level within their respective representative uncertainties: ± 150 K for T_{eff} , ± 0.30 dex for $\log g$, ± 0.20 km s⁻¹ for v_{mic} and an adequate uncertainty on the continuum level depending on the line density and the apparent rotational velocity of the star analysed. The abundance was then altered until the fit

⁷Recall: $[\frac{X}{H}] = \log_{10} \left(\frac{X}{H} \right)_{\star} - \log_{10} \left(\frac{X}{H} \right)_{\odot}$

to the observed profile was achieved again. This yields the abundance response to the slight change in effective temperature, $\sigma_{T_{\text{eff}}}$, surface gravity, $\sigma_{\log g}$, microturbulent velocity, $\sigma_{v_{\text{mic}}}$ and continuum placement, σ_{cont} respectively. Assuming these various responses are independent, we then calculated the total uncertainty on the mean abundance deduced as follows:

$$\sigma_{\text{tot}} = \sqrt{\sigma_{T_{\text{eff}}}^2 + \sigma_{\log g}^2 + \sigma_{v_{\text{mic}}}^2 + \sigma_{\text{cont}}^2}.$$

The final adopted uncertainties are listed in Table 9, 10, and 11 for B-, A-, and F-type stars, respectively. This error analysis is similar to those performed by Varenne & Monier (1999), Fossati et al. (2009) and Santrich et al. (2013).

4. Results

4.1. Abundance patterns

Abundance pattern graphs where abundances are displayed against atomic number Z are particularly useful for comparing the behaviour of the abundances of various elements for B, A and Am, F and Fm stars. The abundance patterns of late B-, A- and F-type stars with $v_e \sin i \leq 150 \text{ km s}^{-1}$ are shown in Fig 5, 6 and 7, respectively with representative error bars. Inspection of these figures shows that, while the abundances of the F stars tend to be almost identical within the error bars, the abundances of the A and late B-type stars show larger and real star-to-star differences for a few chemical elements. The abundance patterns of the 2 Am stars (NGC 6405 47, Am) and NGC 6405 05 (mild Am) exhibit the characteristic sawtooth pattern of Am stars with a marked deficiency of scandium and overabundant elements heavier than titanium. We stress that the existence of star-to-star variations of the abundances can be established independently of the errors in the absolute

values of the oscillator strengths, since all stars will be affected in the same manner.

4.1.1. *Star-to-star abundance variations*

In order to quantify the star-to-star variation of the abundances for a given element, we calculated the average abundance of that element and its standard deviation for the A- and F-type stars in M6 (Table 12). We did not perform this exercise for the late B-type stars as most of them are very fast rotating stars ($v_e \sin i > 150 \text{ km s}^{-1}$) and the errors on the abundances are much larger for these stars because of the uncertainty on the continuum placement.

Among the normal A-type stars, the largest star-to-star variations occur for Ba ($\pm 0.31 \text{ dex}$), Y ($\pm 0.19 \text{ dex}$), Mg ($\pm 0.18 \text{ dex}$) and Mn ($\pm 0.17 \text{ dex}$). The star-to-star variation of $[\text{Ba}/\text{H}]$ is much larger than the error on its abundance ($\pm 0.19 \text{ dex}$), while the spreads of $[\text{Y}/\text{H}]$, $[\text{Mg}/\text{H}]$ and $[\text{Mn}/\text{H}]$ are slightly larger than the maximum abundance uncertainties which we derived for fastest rotating stars for these elements. We therefore believe that the star-to-star variations in the abundances of these elements are real. The abundances of Oxygen, Silicon and Calcium exhibit smaller star-to-star variations ($\sim \pm 0.1 \text{ dex}$), which still remain larger than the uncertainties of their abundances.

For the normal F-type stars, the star-to-star abundance variations of the elements are mostly less than $\pm 0.1 \text{ dex}$, which is smaller than the typical uncertainties of the derived abundances. Only the Fm type star no. 69 exhibits a slightly different pattern than the other F stars in particular differences in the Calcium, Chromium, Manganese, Iron, Yttrium and Barium abundances. This stems from the Fm character of this star. We thus fail to find any clear evidence for star-to-star variation of the abundances for normal F stars, while the normal B and A stars tend to display larger star-to-star variations than F stars.

4.1.2. *The average metallicity of the cluster*

The F-type main sequence stars, which have substantial convective envelopes, have mixed outer layers. Their abundance patterns should thus reflect the initial chemical composition of M6.

For each chemical element, the derived mean abundances for the chemically-normal F-type stars of M6 are collected in column 8 of Table 12, together with their standard deviations. These mean abundances are not significantly different from solar abundances, except for Ba which is found to be overabundant (+0.53 dex). Magnesium, Si, Cr and Fe exhibit only marginal overabundances, which do not exceed 1.4 times of solar abundances. From this, we infer that the initial composition of M6 was nearly solar.

The mean iron abundance of M6 is found to be $[\text{Fe}/\text{H}] = 0.07 \pm 0.03$ from the individual iron abundances of the seven normal F stars. The mean iron abundance can be used to derive the metallicity Z of M6 using the following relation (see Fossati et al. 2011):

$$Z_{\text{cluster}} = Z_{\odot} 10^{([\text{Fe}/\text{H}]_{\text{Fstars}})} .$$

Using a solar metallicity of $Z_{\odot} = 0.017$ (Grevesse & Sauval 1998), the derived $Z = 0.022 \pm 0.001$ for M6 is only marginally larger than the solar metallicity. It is also slightly larger than the present day metallicity, 0.014 ± 0.002 , derived from young early type B stars in the solar vicinity by Nieves & Przybilla (2012). This suggests that M6 formed in an environment slightly enriched in metals compared to the current solar neighbourhood.

4.1.3. Behavior of the abundances with stellar parameters

As we did previously for the other open clusters, we have investigated the behavior of the elemental abundances against effective temperature, projected rotational velocity and the iron abundance. Any correlations/anticorrelations between the abundances and these atmospheric parameters will provide valuable constraints to theorists investigating the various hydrodynamical mechanisms affecting photospheric abundances. The abundances of the iron-peak elements, in particular manganese, should increase with effective temperature if radiative diffusion is efficient. Up to a rotational velocity of about 120 km s^{-1} , the abundances should not depend on $v_e \sin i$ and may decrease at higher velocities (Charbonneau & Michaud 1991).

Figs. 8, 9 and 10 display the abundances of C, O, Mg, Si, Ca, Ti, Cr, Mn, Ni, Sr, Y and Ba as a function of T_{eff} with representative error bars. The profiles of the abundances of C, O, Mg, Ca, Ti, Cr, Mn and Sr are flat within $\pm 2 \sigma$ of the mean abundance of the element, ie. their abundances are not correlated to the effective temperature. For the normal stars, [Si/H] slightly decreases for the hottest stars only (based on 3 data only). The [O/H] and [Mn/H] profiles are flat but exhibit slightly more scatter than the other elements. One should note that [Ni/H], [Y/H], and [Ba/H] increase with T_{eff} at $T_{\text{eff}} > 8500 \text{ K}$, but these trends are based on 3 data only.

No correlations either were found between the abundances and $v_e \sin i$. All abundance profiles against $v_e \sin i$ are flat within $\pm 2 \sigma$ of the mean abundance of the element, with more or less scatter. This behaviour is expected as simulations of the abundance patterns in presence of rotation showed that abundance should not depend on rotational velocities at least up to 120 km s^{-1} since the timescale of diffusion are much shorter than those of rotational mixing (Charbonneau & Michaud 1991).

The abundance ratios [Ti/Fe], [Cr/Fe], [Mn/Fe], [Ni/Fe], [Y/Fe], and [Ba/Fe] appear

to be correlated with the abundance of Fe, while those of C, O, Mg, Si, and Sc are anticorrelated with $[\text{Fe}/\text{H}]$ (see Fig. 11). Table 13 collects the coefficients of the regression analysis. Note that the abundances of magnesium and calcium do not show any convincing correlation nor anticorrelation against $[\text{Fe}/\text{H}]$.

5. Discussion

5.1. Comparison with previous studies

In this section, we compare the abundance patterns found for M6 with those found for the other open clusters: Praesepe, NGC 5460, Coma Berenices, the Pleiades and the Hyades analysed by Fossati et al. (2007), Fossati et al. (2011), Gebran et al. (2008), Gebran & Monier (2008), Gebran et al. (2010), respectively.

The analysis of these clusters revealed a common trend: the star-to-star variations of the abundances of most chemical elements are usually larger for A stars than for F stars. In their analysis of Coma Berenices (age about 450 Myr), Gebran et al. (2008), found that the A stars exhibit larger star-to-star variations for C, O, Na, Sc, Ti, Mn, Fe, Ni, Sr, Y, Zr, and Ba, than the F stars do. For the Pleiades (age about 100 Myr), Gebran & Monier (2008) showed also that A stars exhibit larger variations in C, Sc, Ti, V, Cr, Mn, Sr, Y, Zr and Ba, than the F stars. For the Hyades (age about 700 Myr), Gebran et al. (2010) found significant star-to-star variations of the abundances of C, Na, Sc, Fe, Ni, Sr, Y, and Ba for the A stars (ie. the maximum abundance spread is larger than three times σ , the representative uncertainty on the mean abundance of the considered element). Our findings for the M6 open cluster (age about 75 Myr) similarly confirm that normal A stars exhibit a larger scatter of their abundances around the cluster for Mg, Si, Ca, Cr, Mn, Fe, Y, Ba, than the F stars do. We note that the Cr, Mn, Fe, Y, and Ba abundances exhibit

significant star-to-star variations among the normal A stars for each cluster. We believe that these variations can be interpreted as evidence of transport processes induced by the larger rotation rates in these stars and competing with radiatively driven diffusion.

Similarly, the anticorrelations of $[\text{C}/\text{Fe}]$, $[\text{O}/\text{Fe}]$, $[\text{Mg}/\text{H}]$, $[\text{Si}/\text{H}]$ and $[\text{Sc}/\text{H}]$ with $[\text{Fe}/\text{H}]$ and the correlations of $[\text{Ti}/\text{H}]$, $[\text{Cr}/\text{H}]$, $[\text{Mn}/\text{H}]$, $[\text{Ni}/\text{H}]$, $[\text{Y}/\text{H}]$ and $[\text{Ba}/\text{H}]$ with $[\text{Fe}/\text{H}]$ in M6 can be compared with those found by Gebran et al. (2008) and Gebran et al. (2010) for the Coma Berenices and Hyades cluster in terms of both slope and sign of the regression. Gebran et al. (2008) found correlations between $[\text{Mn}/\text{H}]$, $[\text{Ni}/\text{H}]$, $[\text{Sr}/\text{H}]$, $[\text{Ba}/\text{H}]$ versus $[\text{Fe}/\text{H}]$ and anti-correlations for $[\text{C}/\text{Fe}]$ and $[\text{O}/\text{Fe}]$, for the A and Am stars in Coma Berenices. Our findings for M6 strongly support these findings: $[\text{C}/\text{Fe}]$ and $[\text{O}/\text{Fe}]$ exhibit anti-correlations and most other elements exhibit strong correlations with $[\text{Fe}/\text{H}]$ as predicted by models including diffusion. In particular, we note that the slope of the anticorrelation of $[\text{C}/\text{Fe}]$ vs. $[\text{Fe}/\text{H}]$ in Fig 11, which equals to -1.20 for M6, is only slightly larger than -1.74 found by Gebran et al. (2008) for 15 A and F stars in Coma Berenices and agrees well with -1.24 found by Hill (1995) for 15 sharp-lined field A stars.

5.2. Comparison to the predictions of self-consistent evolutionary models

5.2.1. The Montréal OPAL-based stellar evolution code

The derived abundances have been compared to the predictions of recent evolutionary models computed with XEVOL, the Montréal stellar evolution code⁸. This code evolved from a lagrangian stellar evolution code written by D. A. VandenBerg and the Victoria Group (Pedersen et al. (1991)). Proffitt & Michaud (1991a,b) added an accurate, implicit treatment of atomic diffusion (including thermal diffusion) and gravitational settling of

⁸From the Georges Michaud astrophysics group.

all major isotopes of H, He, C, N, and O, and some trace elements (Li, Be, B); various simple expressions were used to compute radiative forces on a few test elements. They also introduced and explored the effects of a simple density power-law model of *turbulent diffusion*, as a means of smoothing composition discontinuities near convection zone boundaries, in a physically reasonable and parametrizable way.

The Victoria code relied on multi-dimensional interpolation among pre-calculated Rosseland opacity tables, like most stellar codes of that time. One of the most promising sets of opacity tables was the set developed entirely from theory by the OPAL project (Rogers & Iglesias 1992); this and many other similar alternatives were used and compared by different authors for many years; they all had a common weakness: they did not provide a means of reliably computing radiative forces *on-the-fly*. Some XEVOL experiments were made with the GLAM method of radiative force calculations⁹ (Gonzalez et al. 1995) but the method is too time-consuming for stellar evolution applications.

Richer et al. (1998) introduced into XEVOL the new OPAL96 opacity data provided by Iglesias & Rogers (1996); these contain not only OPAL’s new Rosseland mean opacity tables, but also the full spectra of all elements in their mix, at all tabulated points, plus tables of the average ionic charge of each element¹⁰. These allow the easy computation of various mean opacities and radiative accelerations at any point in the star, for any local composition. The spectra of all elements (24 distinct atomic numbers are currently available¹¹) are separately given for standard abundances and standard temperatures and densities (using $R \equiv \rho/[T/10^6 \text{ K}]^3$ as the density variable), on a common 10^4 -point grid of

⁹This method can be used for any atom whose basic atomic data are known.

¹⁰Average ionic charges are used to setup diffusion equations in terms of *average ions*, for elements other than H or He.

¹¹of which three (Li, Be, B) were computed by the Montréal group, not by OPAL.

the dimensionless frequency $u \equiv h\nu/kT$.

Elemental spectra are first scaled according to the local abundances of the stellar model shell, on each point of a small (T_i, R_j) sub-grid¹² of the OPAL96 tables bracketing the actual (T, R) parameters of the shell; the spectra are then added, inverted as necessary, then integrated over frequencies; the resulting local sub-grid values for the function $(\kappa_R, g_{\text{rad}}(\text{element}))$, or other property of the plasma under consideration) are then combined using the electronic density N_e and temperature T as interpolation variables (a requirement of the OPAL *method of corresponding states*)¹³, to compute the desired local quantity at the layer (T, R) ; local radiative accelerations and mean opacities (and their thermodynamic derivatives) are calculated in this way. This is repeated at each model layer and for each time step, and repeated as necessary until convergence of the model equations are satisfied everywhere. Such calculations were not possible until the advent of fast and inexpensive parallel computers.

Radiative accelerations include corrections factors for the redistribution of momentum among ionization states from Gonzalez et al. (1995) and LeBlanc et al. (2000); these become progressively more important as one approaches the star surface, and are not computable from OPAL data.

Turcotte et al. (1998a,b) introduced finite element methods early in the development of the Montréal code, to improve the treatment of diffusion (element conservation in conditions

¹²Usually of size 2×2 , for speed. To each (T_i, R_j) pair correspond 24 spectra of individual elements, plus other plasma properties, at standard abundances.

¹³Integrations must be performed before interpolations, as explained by Richer et al. (1998), because of the T dependence of physical frequencies corresponding to given dimensionless frequencies u .

of extreme concentration variations) and to extend it to all elements in the model; they adapted it to allow accretion and pulsation studies; Vick et al. (2010) added the handling of *mass loss*, either homogeneous or inhomogeneous¹⁴. The evolution code was modified to allow diffusion physics to cover the whole envelope, right up to the atmosphere, the first surface layer (and model outer boundary) being allowed to be as thin as $10^{-15} M_{\odot}$. New turbulence models and new parameterizations were introduced; the latest version of the code allows for multiple, uncoupled or weakly coupled turbulent zones bordering convection zones. This makes possible the study of some hot main sequence stars, where the outer envelope is thought to harbor a complex multi-zone convective structure.

5.2.2. Modeling of the P-rich star HD 318101

We have specifically attempted to model the abundance pattern of HD 318101 (cf. Sec A.2.3), which we identify as a new P-rich star in M6. This star belongs to the He-weak/Hg-Mn region of the HR diagram (cf. Fig. 1.1 and Sect. 8.1–8.3 of Michaud et al. (2015) for a general discussion of diffusion phenomena in these stellar classes).

A proper simulation of element diffusion in this type of stars requires a detailed analysis of radiative forces and diffusion in the atmospheric layers of the star; unfortunately, XEVOL is of limited help in *stable, optically thin* atmospheric layers, which appear to be playing a major role in the development of HD 318101 surface anomalies; the code only knows about LTE physics, the diffusion approximation of the radiative transfer problem,

¹⁴Major modifications to the mesh control and optimization algorithm now allow the evolution to proceed through the He-flash (with a simplified treatment of the flash event itself) to the first half of the Horizontal Branch evolution, the code current limit corresponding to the time when both H and ^4He are completely destroyed in the star center ($X = Y = 0$).

and cannot deal with non-local atmospheric radiative transfer. Nevertheless, we assume it still gives a reasonable working approximation for the overall structure of the atmosphere, but our radiative forces and abundance profile solutions cannot be trusted there, as illustrated convincingly by the work of Alecian & Stift (2010) and Alecian et al. (2011), and summarized in Michaud et al. (2015, § 8.1–2). For that reason, XEVOL has until now only been applied to cases where atmospheric layers could be assumed to be well mixed at all times by some turbulence generating mechanism (e.g., a nearby convection zone). The optically thick parts of the star should be well modeled by XEVOL.

In the case of HD 318101, XEVOL can predict the evolution of element distributions in the stellar core and envelope, and give, if so desired, quantitative information about the initial *flux* of each element into atmosphere, through the atmosphere/envelope boundary.

Once the evolution of the inner parts are sufficiently well characterized, the atmospheric layers could be handled in a way similar to the approach of Moehler et al. (2014) or Alecian & Stift (2010), to obtain a complete solution (some iterations of the whole process may be necessary for fine tuning of M_* , L_* and $T_{\text{eff}*}$ at the desired ages). The simulation data shown below must be considered as a first approximation to the solution.

The mixing length parameter and the initial He abundance for our HD 318101 models ($\alpha = 2.096$ and $Y_0 = 0.279$ respectively) were calibrated to fit the current luminosity and radius of the Sun (see Turcotte et al. 1998b, model H). The models follow the evolution of all its elements, including a few of their isotopes (^2H , ^3He , ^6Li , ^7Li , ^9Be , ^{10}B , ^{11}B , ^{13}C), up to nickel. Models were evolved from the pre-main sequence with a solar scaled metals mixture (these initial abundances are listed in Table 1 of Turcotte et al. 1998b). The initial (zero age) mass fraction of metals was set to $Z_0 = 0.02$. In models with little or no mass loss, the atmospheric layers must be kept homogeneous to prevent excessive buildup of some elements at the surface, as a result of their large outward fluxes, and because of the

limitations of our atmosphere modeling as we have just explained above; this was done numerically from the surface down to a temperature of 65 000 K, at every time step; the interior limit corresponds to the He II convection zone.

The self-consistent modeling proceeds as described in Richer et al. (2000); turbulence is needed to prevent excessive anomalies to develop very rapidly even in the envelope. Various profiles have been used in a search for conditions that would allow phosphorus and other elements to rise to the surface, while maintaining a near normal iron abundance at the age of the star; we allowed in our search an age window of 50–100 Myr. A temporary rise in Fe would be acceptable as long as it returned near solar values at the time of the observations.

In the Richer et al. (2000) study, only one surface “convection” zone was considered: a zone including all mass from the surface down to the inner boundary of the deepest surface zone (it could be the He II or the Fe convection zone inner boundary). To the assumed complete mixing in this large convection zone, turbulence below the zone was added in the form of a turbulent diffusion coefficient, D_T , according to various profiles and only down to layers where atomic diffusion becomes dominant over turbulent diffusion. The cause of this turbulence was not considered.¹⁵ In these conditions, it was shown that the resulting anomalies only depend on the initial metallicity plus one extra parameter that was called the “effective mixed mass”, not on the detailed shape of the turbulence profile. Fig. 12 of that article shows abundance patterns for a star of $2.5 M_\odot$ starting with $Z_0 = 0.02$; the models all share a similar P overabundance typically in the +0.3 to +0.7 dex range. Their Fig. 14 shows that $[\text{Fe}/\text{H}]$ tends to saturate at about +0.3 dex (taking into account the rise in H), while the P rise does not saturate; it follows Fe at 100 Myr, but continues to rise as evolution continues; Fig. 22 shows one case where the P abundance anomaly is about twice

¹⁵It was found to be compatible with rotationally induced turbulence as calculated by Zahn (2005) and Talon et al. (2006).

that of Fe; but this is in an older and cooler star ($T_{\text{eff}} = 7500$ at 800 Myr).

For the calculations presented here, we considered stellar masses in the range 4.5–5.0 M_{\odot} . Surface homogenization was always applied between the surface and the layer at which $T = 65\,000$ K, to speed up calculations and avoid instabilities in the optically thin regions. This amounts to assuming that the He II convection zone is turbulent enough to eventually mix also all the layers above it in a short time, compared to the lifetime of the star.

Fig. 12 presents the evolution of some internal properties of these models for HD 318101, with masses 4.7 M_{\odot} (red curves) and 5.0 M_{\odot} (blue curves), which should be representative of that star. The Mn-Fe-Ni convection zone was allowed to develop on its own¹⁶, spreading between $\sim 130\,000$ K and $\sim 300\,000$ K, but some mild turbulence was added there, to help manage the proliferation of tiny convection zones in that area, by helping them fuse. The turbulent diffusion coefficients used were of the form (see Michaud et al. 2015, § 7.3.3)

$$D_{\text{T}}(\rho) = \omega D_{\text{He}}(T_0) (\rho/\rho(T_0))^{-3}, \quad (1)$$

where ρ is the local density, $D_{\text{He}}(T_0)$ is the diffusion coefficient of ^4He in hydrogen at $T = T_0$ in the model, and ω is a constant controlling the overall strength of the profile, relative to atomic diffusion of He.¹⁷ The reference T_0 was set to 150 000 K and the turbulence scale ω was set to 1000 in both cases.¹⁸

¹⁶which it did in about 3.5 Myr.

¹⁷Hu et al. (2011) used a similar expression for D_{T} in the context of sdB stars.

¹⁸According to past XEVOL model naming conventions, these diffusion models would be called: M4.7000DiffT150KD1K-3 and M5.0000DiffT150KD1K-3, where the letters M, T, D are followed by the star mass, the turbulence profile anchoring temperature T_0 , and the scale ω and slope of the turbulence profile; often, $\log T_0$ is used instead of T_0 after T. Mass loss

In this short mass range, most red and blue curves look very much like time-stretched copies of each other. The effective temperatures would be compatible with the observed one (within error bars) for an age in the range of 50–70 My. Panels for elements He to Fe show surface concentration changes $\log_{10}(X/X_0)_{\text{element}}$. The convection zone (cz) panels show the depths of all the convection zone boundaries in the atmosphere and the envelope, in the course of time. M_{cc} is the convective core size, in solar masses.

P and Fe follow each other closely, as in the less massive Richer et al. (2000) models mentioned above, but with P climbing slightly more than Fe. The observable abundances (taking atmosphere physics into account) would depend on how these large overabundances redistribute themselves within the atmosphere, in a locally stratified structure; some Fe may actually be ejected from the surface while P, having fewer supporting lines, may remain trapped there, leading to the observed pattern in HD 318101.

Fig. 13 shows the g_{rad} profiles of a number of elements in the $4.7 M_{\odot}$ T150KD1K-3 model, at what are roughly the beginning (50 Myr, grey), and the end (85 Myr, red) of the age window considered acceptable for HD 318101. Profiles are also shown prior to the appearance of the Mn-Fe-Ni convection zone, at age 2 Myr (green curves). The evolution towards the right of all the curves is the result of the cooling of envelope layers during that period. The limits of the He II and Mn-Fe-Ni convection zones are indicated by vertical bars (*dotted* for He and *solid* for Mn-Fe-Ni). One notices a marked difference between P and Fe behaviour in the vicinity of the He convection zone, with P being more strongly pushed towards the surface in that region; P also appears to be wanting to leave the star, while Fe does not; but as explained above, the atmospheric part of the model is not sufficiently reliable to draw such conclusions, especially in the present case where

(stellar wind) is labelled W, when present. This convention is also adopted in the present article; we will use shortened names whenever context allows it.

$g_{\text{rad}}(\text{P}) \approx g_{\text{rad}}(\text{Fe}) \approx g$ in these layers after 50 Myr. The weak $g_{\text{rad}}(\text{Fe})$ in the upper envelope is in good part the result of lines saturation; we see that Cr, Mn, and Ni are less affected by it, due to their lower abundance. As time passes, a given peak of the deeper force profile of an element pushes that element up with a decreasing force, into an increasing amount of mass. Elements P and Fe are both pushed into the Mn-Fe-Ni convection zone from below; P should accumulate there, but not Fe, which continues to rise towards the surface. Phosphorus within the topmost $\sim 10^{-8} M_*$ of the envelope should also rise towards the surface, potentially allowing overabundances in excess of a factor 10^3 to 10^5 , limited by a growing opposite diffusion gradient in the atmosphere (or by mass loss, if there were some); it is line saturation which prevents Fe from growing even more than P at the surface.

Fig. 13 suggests that one might be able to reproduce the P and Fe abundances of HD 318101 (high P, normal Fe) if one can avoid mixing surface layers down to the bottom of the He II convection zone, and stop evolution at an early age (e.g., ≤ 50 Myr). This would require extremely short time steps, and keeping the Mn-Fe-Ni convection zone well mixed to prevent that region from taking control over the evolution.

Convection zones

Richard et al. (2001) looked at convection zones caused by iron-group elements in main-sequence stars of various metallicities ranging from $Z_0 = 0.01$ to 0.03 . Their Fig. 8c shows the full evolution of convection zones in a $2.5 M_\odot$ star. The iron convection zone (labelled γ in their figure) is getting wider with increasing stellar mass. The situation in HD 318101 follows that trend, but appears to be more complex, probably due to its higher mass and effective temperature, and shorter diffusion timescale (Richard et al. 2001; Richard 2005). The most important obstacle to simulation is the chaotic convective structure that develops when Fe, Mn, and Ni become abundant enough to trigger convection; these elements are

subject to radiative force saturation, which limits their overabundances in “iron-group” convection zones, but also leads to their spreading (as shown by Richard et al. 2001); this is illustrated here in Fig. 14 for tentative models for star HD 318101. The detailed structure of these convection zones, whether they lump together or split into many parts, depends sensitively on the shapes of the rapidly changing Fe, Mn, and Ni abundance profiles. Numerical noise in these profiles can contribute to the convection zone(s) fragmentation; some of that noise originates in the bilinear (R, T) interpolation method used with OPAL grid data. Some localized turbulence is introduced to help smooth out that evolution.

Three simulations are shown. The first one is T65KD10-4 (blue), with weak, short range turbulence limited to the hot boundary of the He II convection zone; model T150KD1K-3 (grey) has much stronger turbulence effectively limited to the Mn-Fe-Ni convection zone only (grey); finally, model T65KD30-4W5E-15 (red) has turbulence 3 times the strength of that in the blue model, plus weak, constant stellar mass loss ($5 \times 10^{-15} M_{\odot}/\text{yr}$) introduced to peel off the topmost layers of the star, where excessive accumulation of some elements may occur. The chaotic pattern found at around 4 Myr grows and doubles in width by age 20 Myr, then persists for the rest of the main-sequence life of the star; it covers more than a factor of 10 in envelope mass $\Delta M/M_*$ ¹⁹. The Mn-Fe-Ni convection zone eventually extends from $\log T = 5.10$ to 5.45 in the grey model, which evolves more smoothly thanks to this well mixed, single “iron-group” convection zone; that simulation also appears as the red curves in Fig 12. Note that in all three models, homogeneity is also artificially imposed by mixing, in all the layers between the surface and the He II convection zone.

In every case, one finds a massive extended region of marginal convective stability, that the code tries to monitor in detail, when some average solution might be more appropriate physically and easier to use numerically; this complexity prevented the simulations with

¹⁹ ΔM is the envelope mass, measured from the surface

weak turbulence from continuing. The low mass loss used did not affect significantly the “iron-group” convection zone; higher mass loss rates would have to be investigated, but that would still not help solve the atmosphere problem, and in the present case, would reduce both P and Fe in the same way, unless inhomogeneous mass loss were introduced; this was not attempted since implementing a more realistic atmosphere solution must be done first.

Predicted surface composition

In Fig. 15 we compare the predicted surface abundances of all the main elements handled by XEVOL for two models of mass $M_* = 4.7 M_\odot$, with independent measurements from Monier (2014, private communication) and Kılıçoğlu et al. (this paper) for the P-rich star HD 318101. Nine different ages are shown from the evolution of model T150KD1K-3 of Fig. 12 and 14; these cover the whole main-sequence lifetime of the star; a single age is shown for model T65KD10-4 (blue points in Fig. 14).

The results do not depend sensitively on the stellar mass; a range of masses (we looked at 4.5–5.0 M_\odot), effective temperatures, and ages are possible around these values, but all share very similar abundance profiles, with strong positive correlation between P and Fe (see also Fig. 12). This can be tracked down to the similarity of the $g_{\text{rad}}(\text{P})$ and $g_{\text{rad}}(\text{Fe})$ profiles (see Fig. 13), which remain almost identical in shape and strength in the deep envelope, throughout the evolution; the only noticeable difference is in the smoothness of these profiles: the P profile becomes noisier as we approach the surface; this is caused by the much smaller number of lines in its spectrum. The P abundance rises very rapidly then remains constant for almost the whole evolution; the iron-peak elements (Mn, Fe, Ni) also rise very quickly, then decrease slowly and steadily until about 90 Myr. Unfortunately, this decrease is not quick enough to return Fe to near solar level while P is still high. As mentioned at the beginning of § 5.2.2, we expect the huge quantities of P and Fe pushed

towards the surface to be further stratified in the atmosphere, in different ways, leading to the observed difference, but this cannot be proved with XEVOL alone.

All elements $\leq \text{Ca}$, except phosphorus, appear to fit the predicted patterns very well in the age range 45–95 Myr, given the quoted error bars. As discussed at the end of § modelingHD318101, the high P abundance may also agree with models which do not enforce mixing down to the He convection zone (still do be demonstrated). Some measurements suggest P might actually be lower in HD 318101 and closer to the 1.1 mark, in which case the match would be perfect.

Uncertainties in $g_{\text{rad}}(\text{P})$ calculations

Besides error bar estimates on observations, theoretical models themselves have uncertainties of their own in their radiative force calculations; the latter are necessarily propagated to the predicted abundances of the models. Uncertainties about the physics (plasma equation of state, core-electron approximations, quantum cross-sections, etc) have been discussed by the authors of the OPAL tables. Uncertainties originating from the use of frequency sampling are *not* known, and may be the most important ones, as far as g_{rad} calculations are concerned. They are of two types: 1) errors due to insufficient spectrum resolution; 2) errors due to unknown relative positions of lines of different elements.

LeBlanc et al. (2000) studied in a quantitative way the importance of frequency grid resolution on the calculation of $g_{\text{rad}}(A)$, and showed its effects for ten elements A in the OPAL database (but unfortunately not phosphorus); their Fig. 4 shows the effect of using low resolution spectra (10 000 points, non-uniform, optimized for the black body distribution – see their Appendix A), compared to a uniform 10^6 -point u reference grid

covering the same range²⁰; the low resolution and the evaluation temperature (100 000 K) are both similar to the conditions in the corresponding XEVOL evaluation of $g_{\text{rad}}(\text{P})$ in the stellar regions where it is maximum. They verified that phosphorus has very few absorption lines at that temperature in the star, so frequency sampling at the OPAL resolution has a high probability of missing the cores of most of these lines, a situation which reminds one of the case of Lithium. We expect $g_{\text{rad}}(\text{P})$ to carry a similar uncertainty as $g_{\text{rad}}(\text{Li})$, in these stellar layers. These are errors of the *first type* mentioned above.

Errors of the *second type* occur when the absorption spectrum contains a huge number of lines of some abundant element and one needs to compute the light momentum absorbed by another element with very few absorption lines. The light available to that second element is blocked by the huge number of lines of the first element absorbing most of the momentum; since any of these lines carries a large positional uncertainty (typically $\sim 1\%$ in the OPAL database), we don't know for sure what flux should be available in any of the few lines we are considering. This kind of uncertainty is not reduced by increasing resolution; it could be reduced only by increasing wavelength accuracy for all elements.

Richer & Michaud (2005) studied the uncertainty on $g_{\text{rad}}(\text{Li})$ resulting from the uncertainty in the relative positions of Li and Fe absorption lines in the OPAL database²¹. Using a statistical simulation of possible OPAL-like line placements errors, these authors were able to show that $g_{\text{rad}}(\text{Li})$ values at particular temperatures can vary by large factors (cf. Fig. 3 and 4 of Richer & Michaud 2005); in the worst cases, these factors could *typically*

²⁰The 10^6 -point calculation was shown, through more exact methods of evaluation (analytical line profile integrations), to be accurate to better than 0.1% on the resulting $g_{\text{rad}}(A)$, for all A studied

²¹This problem is very similar to the one discussed in Sections 3 and 4 of LeBlanc et al. (2000).

be

$$g_{\text{rad}}(\text{Li})_{[\text{true}]} = (0.2 \text{ to } 3.) \times g_{\text{rad}}(\text{Li})_{[\text{frequency sampling}]} . \quad (2)$$

The resulting diffusion velocity of the element would be uncertain by the same factor; the abundance itself depends exponentially on this velocity in many transients situations, and its uncertainty could be much greater. One should repeat this analysis in the case of phosphorus, to clarify the predictions of XEVOL+OPAL calculations for that element. If the same level of uncertainty applies to P in the envelope of HD 318101, the theoretical predictions of the present paper, augmented by this sampling uncertainty factor, will be well within the range of measured values.

LeBlanc et al. (2000) were able to show that for elements such as Fe, the huge number of lines available allows the frequency sampling method to produce a statistically unbiased estimate of $g_{\text{rad}}(\text{Fe})$.

Other models

Differentiated mass loss (inhomogeneous wind) could play a significant role in the evolution of surface abundances of some elements in HD 318101. It would be possible to use the present XEVOL model to test this inhomogeneous wind model as a mean of getting rid of the Fe atmospheric excess, while retaining most of the phosphorus at the surface. Only preliminary work has been done in that direction so far.

6. Conclusions

The spectra of 44 late-B, A, and F dwarfs of M6 have been synthesized in a uniform manner to derive LTE abundances of up to 20 chemical elements. This is the first extensive abundance study of intermediate mass stars in M6 with stars ranging from $1.4 M_{\odot}$ up

to $4.3 M_{\odot}$. As we did for other open clusters, we find that the abundances of several chemical elements exhibit real star-to-star variations in the B and A stars, larger than for the F stars. The largest spreads occur for [Mg/H], [Mn/H], [Y/H] and [Ba/H] while the smallest are for [Si/H], [Ca/H], [Sc/H], [Ti/H], [Cr/H], [Fe/H] and [Ni/H]. The derived abundances do not show clear systematic trends with effective temperature, nor with apparent rotational velocities as expected since the timescale of diffusion are much shorter than those of rotational mixing (Charbonneau & Michaud 1991). The relative abundances [Ti/Fe], [Cr/Fe], [Mn/Fe], [Ni/Fe], [Y/Fe], and [Ba/Fe] are correlated with that of iron and the relative abundances [C/Fe], [O/Fe], [Si/Fe], and [Sc/Fe] are anticorrelated with [Fe/H] as expected from models including diffusion. The normal F stars have nearly solar abundances for almost all elements with little scatter around the mean abundances. In these stars, Mg, Cr and Y are only marginally overabundant and Ba is overabundant. These results agree quite well with the findings of the previous extensive abundance surveys of Gebran et al. (2008), Gebran & Monier (2008), and Gebran et al. (2010) for Coma Berenices, the Pleiades and the Hyades.

In the course of this analysis, we have discovered five new chemically peculiar stars of different types in M6. Stars 5, 47, and 69 appear to be a mild-Am, an Am and a Fm star respectively, star 99 is a new HgMn star, and star 20 (HD 318101) is a new He-weak and P-rich star.

The detailed modeling of the P-rich star HD 318101 including radiative forces and different amounts of turbulent diffusion reproduces the overall shape of the abundance pattern for this star and the abundances of the light elements He, C and O but not those of heavier elements, in particular the iron-peak elements. Models with the least turbulence reproduce the abundances of the lightest elements ($Z < 12$) and those with most turbulence reproduce coarsely abundances of elements with $Z > 15$ (assuming an age in the 50–90 Myr

range).

The discrepancies between derived and predicted abundances appear to come from the stratification of some elements in the atmosphere of that star, a phenomenon which is not handled by the XEVOL code, and requires more realistic (non local) radiative transfer calculations. However, the manner in which radiative forces change over time in our models for HD 318101 suggests another solution: a very young model (~ 50 Myr) may actually fit most observations (including the phosphorus and Fe-group abundances) if no mixing is introduced far from the convection zones and in particular, at the surface. Such a model still needs to be investigated with XEVOL, but would certainly be numerically challenging.

Acknowledgment. This work and the first author was supported by TÜBİTAK (The Scientific and Technological Research Council of Turkey) under Program No. 2214 (2011-1).

A. Appendix material

A.1. Radial velocities

The radial velocity of each star was derived by cross-correlating each observed spectrum with an appropriate synthetic spectrum computed for the T_{eff} , $\log g$, $v_e \sin i$, v_{mic} , and chemical composition of the star. The radial velocity obtained for each star is listed in Table 14.

We have derived an average cluster radial velocity by weight averaging the radial velocity of the single stars, obtaining $V_r = -8.48 \pm 0.17 \text{ km s}^{-1}$. This value is in agreement with the cluster radial velocity of $-8.27 \pm 0.45 \text{ km s}^{-1}$, given by Frinchaboy & Majewski (2008) derived using six fiducial cluster members.

M6 was observed with the GIRAFFE H09B setting on two different nights, separated

by six days, allowing us to look for radial velocity variations which could be due to orbital motions. Most stars have stable radial velocities, reproducible to within $\pm 2.74 \text{ km s}^{-1}$, which we can consider the intrinsic precision, $\sigma_{v_{rad}}$ of the measurements. We therefore considered stars displaying differences in V_r much larger than this threshold (ie. larger than $3 \sigma_{v_{rad}}$) as exhibiting significant radial velocity variations.

The star no. 99 presents the largest radial velocity variation ($\sim 38 \text{ km s}^{-1}$) and is therefore likely to be a binary. We have also detected radial velocity shifts above the uncertainty limit of 2.74 km s^{-1} for stars nos. 5, 31, 47, 51, 64, and 130. These stars might be single lined spectroscopic binaries (SB1) as the spectral lines of their companion stars are not visible in the observed spectra.

The spectra of the star no. 33 reveal that this is a double-lined spectroscopic binary (SB2) with components of similar spectral type, because of the similar intensity of the lines of the two stars. The effective temperature derived from Geneva photometry indicated an early-F spectral type. We determined the projected rotational velocities of the two stars using unblended well separated iron lines, obtaining $30 \pm 10 \text{ km s}^{-1}$ and $35 \pm 10 \text{ km s}^{-1}$. The maximum V_r difference between the two stars was $170 \pm 10 \text{ km s}^{-1}$.

A.2. Non-LTE effects and notes on individual elements

In this section, we discuss possible departures from LTE which could affect the abundances of helium, carbon, oxygen, magnesium, silicon, calcium and scandium..

Helium: The helium abundances derived for late-B type stars can be regarded as solar within the uncertainties, except for the star no. 20, which is classified as a He-weak P-rich star. The He abundances were derived from the synthesis of the He I 4713Å, 4921Å, and 5026 Å lines which have very accurate $\log gf$ values. Przybilla et al. (2011) have shown

that for stars cooler than $T_{\text{eff}} \simeq 22\,000\text{ K}$ two of these lines, He I 4713 and 5016 Å, are the least affected by non-LTE effects. We also checked Nieva & Przybilla (2007) where these transitions are studied in LTE and NLTE. The recent analysis of helium lines in the HgMn star κ Cancri by Maza et al. (2014) reveals a significant strengthening of a few He I lines prone to isotopic shifts, eg. $\lambda\,4921\text{ Å}$ and $\lambda\,6678\text{ Å}$ which we have not used to derive the helium abundance in the new HgMn star we found in this study.

The B-type stars analysed here are much cooler than 22 000 K. We believe that the non-LTE corrections for He are within about the abundance uncertainties (i.e., ~ 0.2 dex) and we did not correct our LTE determinations. Note that for the hottest CP4 star no. 20, the correction is negative, and this would make helium even more deficient.

Carbon and Oxygen: We derived the C abundance of the A and F-type stars mainly from four C I lines having quality B and C $\log gf$ values. All stars have nearly solar C abundance, but for the two Am stars which are deficient in carbon. We checked the departures from LTE for the considered C I lines using the analysis of the spectrum of Vega (A0V) in Przybilla et al. (2001b). The largest departure (i.e., -0.04 dex) occurs for the C I 4772 Å line. Given the fairly large uncertainties on the C abundance, the departure from LTE for carbon can be considered to be negligible.

We used several O I lines with $\log gf$ values of quality C+, in particular the multiplet at 5329 Å, to derive the oxygen abundance. Oxygen is either normal or only slightly under-abundant with respect to the solar abundance (Grevesse & Sauval 1998) for the B and A-type stars, while it is underabundant for the star no. 47 (Am). As for carbon, we used Przybilla et al. (2000) to check the departures LTE: non-LTE effects for the lines we analysed do not exceed -0.03 dex and can therefore be neglected..

Magnesium and Silicon: There are four relatively strong Mg I lines in the observed spectra of late-A and F stars: Mg I 4702.991, 5167.321, 5172.684, and 5183.604 Å. The first

three of these lines have oscillator strengths of quality B+, while the last one is of quality A. We noticed that the Mg I 4702.991 line systematically yields abundances which are less than those derived from the other three lines. We suppose that the low abundances derived from this line may be due to an erroneous oscillator strength. We thus preferred to synthesize the triplet Mg I lines at 5170 Å only to derive the magnesium abundance. Przybilla et al. (2001a) showed that the Non-LTE correction is -0.06 dex for Mg I 5172.684, while it is -0.13 dex for Mg I 5183.604, for Vega (A0V). This suggests that our derived Mg abundances may be slightly overestimated. This non-LTE correction will decrease the slightly large Mg abundances of the stars, and bring them to solar-like values. For the B and early-A stars, several Mg II lines are available for synthesis, such as Mg II 4739.593, 4739.709, 5264.220, and 5264.364. (Przybilla et al. 2001a) showed that the non-LTE effects on Mg II lines (between 4500-5800 Å) can be considered as negligible in the case of Vega. We note that the Mg abundance derived from these lines for B and early-A type members are indeed found to be solar (Grevesse & Sauval 1998).

The Si abundance was derived from several Si II lines in the spectra, which are of quality B or D, and was found solar for most members with $T_{\text{eff}} < 12\,000$ K. The abundances, however, seem to be reduced for the hottest stars. Wedemeyer (2001), who performed a non-LTE abundance analysis for Si found that the Non-LTE correction of Si is $+0.05$ dex for Vega for the lines we analysed. Przybilla et al. (2011) have shown that lines of Si II are not influenced by non-LTE effects in stars cooler than about 15000 K. Bailey & Landstreet (2013) performed a few checks on the Si II lines of late B-type stars which support this result.

Calcium: Calcium and scandium are crucial elements since they should be underabundant in Am stars. We could only use a limited number (about four) of lines, for both elements to derive their abundances, as many other lines were too weak to appear in

the spectra.

Each member was found to have nearly solar Ca abundances, except for nos. 5 and 71 which are slightly under-abundant, and for no. 69 which is slightly overabundant (+0.25 dex). No. 5 displaying the lowest [Ca/H] is a mild Am star. The unexpected deficiency of Ca for No. 71, which is a chemically normal star, is probably due to the difficulties to model Ca lines, since this star has $v_e \sin i$ of 135 km s^{-1} . The Ca enrichment in No. 69 is unusual as this star is a most-likely a CP1 (Fm) star. In order to find out whether our results were affected by LTE approximation, we used Sitnova et al. (2014)’s results, including the temperature dependent non-LTE corrections of the Ca II 5001 Å line. According to them, non-LTE corrections of this line is negative and does not exceed -0.03 dex for $5000 \text{ K} < T_{\text{eff}} < 8700 \text{ K}$ (also for $\log g=4$ and $[\text{Fe}/\text{H}]=0.0$). The corrections, however, become positive for higher temperatures, and departures considerably increase for $T_{\text{eff}} > 9000 \text{ K}$, and reach about to $+0.19 \text{ dex}$ at $T_{\text{eff}}=10\,000 \text{ K}$. We thus conclude that the derived Ca abundances for members earlier than A3 type might be slightly underestimated in our LTE approximation.

A.2.1. Comments on particular stars

We discuss here i) the stars which stand out from the Main Sequence in the HR diagram of M6, ii) the newly found Chemically Peculiar stars.

The stars no. 25, 118 and HD 318103 were found to be more luminous, than the other cluster members of similar effective temperatures in the HR diagram of M6 while stars nos. 41 and 95 were found to be less luminous . Unknown binarity can also be the reason of these offsets. The derived radial velocity of the star no. 25 ($-6.76 \pm 1.68 \text{ km s}^{-1}$) differs much from what was derived by Frinchaboy & Majewski (2008, $-24.73 \pm 4.63 \text{ km s}^{-1}$). This

difference may arise from a faint companion star whose lines are invisible in the spectra of the star. Time series observations are clearly needed for no. 25 for confirmation of its duplicity, and for no. 118 and HD 318103 to find out whether they are binaries or not.

We present below the abundance pattern of the newly detected chemically peculiar stars.

A.2.2. NGC 6405 5 (HD 318091)

The abundance pattern of NGC 6405 5 indicates that this star is a mild-Am star. Both Ca and Sc are underabundant while Cr and Ba are overabundant relative to the Sun. The star presents also the lowest C abundance among the analyzed stars. The abundances of Mg, Si, Ti, Fe, Ni, Y are nearly solar within their error limits. Its radial velocity variation also suggests that this star is most likely a binary.

A.2.3. NGC 6405 20 (HD 318101)

This star is the hottest and the brightest star among our program stars. The membership of this star was confirmed by Frinchaboy & Majewski (2008) from its three-dimensional motion. The abundance pattern of NGC 6405 20 indicates that this star is most likely a He-weak P[Ga?] (CP4) star. Its effective temperature and low rotational velocity support this classification (see Kurtz 2000). Although we detected a marked overabundance of P and Xe, we failed to identify Ga lines in this spectral region. A spectrum covering the region 3000-4000 Å would be very valuable to check the existence of Ga lines.

A.2.4. NGC 6405 47 (CD-32 13109)

This is the star with the lowest $v_e \sin i$. This star presents clear Am chemical peculiarities: overabundances of Cr, Mn, Fe, Ni, Y, and Ba and underabundances of C, O and Sc. The Ca abundance is solar within the uncertainties. The radial velocity measurements also indicate that the star is most likely in a binary system.

A.2.5. NGC 6405 69 (GSC 07380-01211)

The abundance pattern of NGC 6405 69 shows that the star is a Fm star. It is slightly enriched in Ca, Cr, Fe, Y and Ba. These peculiarities are not as large as those of classical CP1 stars and there is no deficiency of Sc. We did not find any evidence of duplicity for this star from its radial velocity variations.

A.2.6. NGC 6405 99 (HD 318126)

The abundance pattern of NGC 6405 99 indicates that this star is most likely a HgMn star. We detected overabundances of Ti, Cr, Mn, Ni, Zr, Y, Ba and Hg. We could only synthesize Hg I 5769.593 line to derive the Hg abundance. A spectrum including the Hg II 3983.93 Å lines would be very valuable to determine more accurately its Hg abundance. Its binarity detected from radial velocity variations also supports its HgMn classification.

REFERENCES

- Ahumada, J. A., & Lapasset, E. 2007, *A&A*, 463, 789
- Alecian, G., Richard, O., & Vauclair, S., eds. 2005, *EAS Publications Series*, Vol. 17, *Element Stratification in Stars: 40 Years of Atomic Diffusion. Meeting in Honour of Georges Michaud*, held on June 6–10, 2005 in Château de Mons, France (Les Ulis, France: EDP Sciences)
- Alecian, G., & Stift, M. J. 2010, *A&A*, 516, A53+
- Alecian, G., Stift, M. J., & Dorfi, E. A. 2011, *MNRAS*, 418, 986
- Antalová, A. 1972, *Bulletin of the Astronomical Institutes of Czechoslovakia*, 23, 126
- Bailey, J. D., & Landstreet, J. D. 2013, *A&A*, 551, A30
- Becker, W. 1961, *ZAp*, 51, 151
- Becker, W., & Fenkart, R. 1971, *A&AS*, 4, 241
- Bergeson, S. D., & Lawler, J. E. 1993, *ApJ*, 408, 382
- Bessell, M. S., Castelli, F., & Plez, B. 1998, *A&A*, 333, 231
- Bressan, A., Marigo, P., Girardi, L., et al. 2012, *MNRAS*, 427, 127
- Cameron, L. M. 1985a, *A&A*, 147, 39
- . 1985b, *A&A*, 147, 39
- Carraro, G., Villanova, S., Monaco, L., et al. 2014, *A&A*, 562, A39
- Carrera, R., & Pancino, E. 2011, *A&A*, 535, A30

- Castelli, F., & Kurucz, R. L. 2003, in IAU Symposium, Vol. 210, Modelling of Stellar Atmospheres, ed. N. Piskunov, W. W. Weiss, & D. F. Gray, 20P
- Charbonneau, P., & Michaud, G. 1991, *ApJ*, 370, 693
- Cowley, C. R., & Corliss, C. H. 1983, *MNRAS*, 203, 651
- Crawford, D. L. 1978, *AJ*, 83, 48
- Curry, J. J. 2004, *Journal of Physical and Chemical Reference Data*, 33, 725
- Dias, W. S., Alessi, B. S., Moitinho, A., & Lépine, J. R. D. 2002, *A&A*, 389, 871
- Dias, W. S., Assafin, M., Flório, V., Alessi, B. S., & Líbero, V. 2006, *A&A*, 446, 949
- Dimitrijevic, M. S., & Sahal-Brechot, S. 1984, *A&A*, 136, 289
- Dommanget, J., & Nys, O. 1995, *Bulletin d'Information du Centre de Donnees Stellaires*, 46, 3
- Eggen, O. J. 1960, *Vistas in Astronomy*, 3, 258
- . 1961, *Royal Greenwich Observatory Bulletins*, 27, 61
- Fitzpatrick, E. L., & Massa, D. 1999, *ApJ*, 525, 1011
- Fossati, L. 2014, in *Putting A Stars into Context: Evolution, Environment, and Related Stars*, ed. G. Mathys, E. R. Griffin, O. Kochukhov, R. Monier, & G. M. Wahlgren, 19
- Fossati, L., Bagnulo, S., Landstreet, J., et al. 2008, *A&A*, 483, 891
- Fossati, L., Bagnulo, S., Monier, R., et al. 2007, *A&A*, 476, 911
- Fossati, L., Folsom, C. P., Bagnulo, S., et al. 2011, *MNRAS*, 413, 1132

- Fossati, L., Ryabchikova, T., Bagnulo, S., et al. 2009, *A&A*, 503, 945
- Francis, C., & Anderson, E. 2012, *Astronomy Letters*, 38, 681
- Frémat, Y., Lampens, P., & Hensberge, H. 2005, *MNRAS*, 356, 545
- Frinchaboy, P. M., & Majewski, S. R. 2008, *AJ*, 136, 118
- Fuhr, J. R., Martin, G. A., & Wiese, W. L. 1988, *Journal of Physical and Chemical Reference Data*, 17
- Fuhr, J. R., & Wiese, W. L. 2005, in *CRC Handbook of Chemistry and Physics*, 86th Edition, 10-9310-155 (Edited by D. R. Lide, CRC Press, Boca Raton, FL, 2005)
- Fuhr, J. R., & Wiese, W. L. 2006, *Journal of Physical and Chemical Reference Data*, 35, 1669
- Gebran, M., & Monier, R. 2008, *A&A*, 483, 567
- Gebran, M., Monier, R., & Richard, O. 2008, *A&A*, 479, 189
- Gebran, M., Vick, M., Monier, R., & Fossati, L. 2010, *A&A*, 523, A71
- Gonzalez, J.-F., LeBlanc, F., Artru, M.-C., & Michaud, G. 1995, *A&A*, 297, 223
- Grevesse, N., & Sauval, A. J. 1998, *Space Sci. Rev.*, 85, 161
- Griffin, R. F., & Griffin, R. 1979, *A photometric atlas of the spectrum of Procyon $\lambda\lambda 3140\text{--}7470\text{ \AA}$* (Institute of Astronomy, the Observatories, Cambridge, UK), 182
- Harris, G. L. H. 1976, *ApJS*, 30, 451
- Hibbert, A. 1988, *Phys. Scr*, 38, 37
- Hill, G. M. 1995, *A&A*, 294, 536

- Hu, H., Tout, C. A., Glebbeek, E., & Dupret, M.-A. 2011, MNRAS, 418, 195
- Hubeny, I., & Lanz, T. 1995, ApJ, 439, 875
- Iglesias, C. A., & Rogers, F. J. 1996, ApJ, 464, 943
- Jacobson, H. R., Pilachowski, C. A., & Friel, E. D. 2011, AJ, 142, 59
- Johnson, H. L., Hoag, A. A., Iriarte, B., Mitchell, R. I., & Hallam, K. L. 1961, Lowell Observatory Bulletin, 5, 133
- Jura, M. 1987, ApJ, 313, 743
- Kelleher, D. E., & Podobedova, L. I. 2008a, Journal of Physical and Chemical Reference Data, 37, 1285
- . 2008b, Journal of Physical and Chemical Reference Data, 37, 267
- Kharchenko, N. V., Piskunov, A. E., Röser, S., et al. 2009, A&A, 504, 681
- Kramida, A., Yu. Ralchenko, Reader, J., & and NIST ASD Team. 2013, NIST Atomic Spectra Database (ver. 5.1), [Online]. Available: <http://physics.nist.gov/asd>. National Institute of Standards and Technology, Gaithersburg, MD.
- Kunzli, M., North, P., Kurucz, R. L., & Nicolet, B. 1997, A&AS, 122, 51
- Kupka, F., Piskunov, N., Ryabchikova, T. A., Stempels, H. C., & Weiss, W. W. 1999, A&AS, 138, 119
- Kupka, F. G., Ryabchikova, T. A., Piskunov, N. E., Stempels, H. C., & Weiss, W. W. 2000, Baltic Astronomy, 9, 590
- Kurucz, R. 1993, ATLAS9 Stellar Atmosphere Programs and 2 km/s grid. Kurucz CD-ROM No. 13. Cambridge, Mass.: Smithsonian Astrophysical Observatory, 1993., 13

- Kurucz, R. L. 1992, *Rev. Mexicana Astron. Astrofis.*, 23, 45
- Kurucz, R. L., & Avrett, E. H. 1981, *SAO Special Report*, 391
- Kurucz, R. L., & Peytremann, E. 1975, *SAO Special Report*, 362
- Landstreet, J. D., Bagnulo, S., Andretta, V., et al. 2007, *A&A*, 470, 685
- Lanz, T., Dimitrijevic, M. S., & Artru, M.-C. 1988, *A&A*, 192, 249
- Lawler, J. E., & Dakin, J. T. 1989, *Journal of the Optical Society of America B Optical Physics*, 6, 1457
- LeBlanc, F., Michaud, G., & Richer, J. 2000, *ApJ*, 538, 876
- Lindoff, U. 1968, *Arkiv for Astronomi*, 5, 1
- Ljung, G., Nilsson, H., Asplund, M., & Johansson, S. 2006, *A&A*, 456, 1181
- Maitzen, H. M., & Schneider, H. 1984, *A&A*, 138, 189
- Martin, G. A., Fuhr, J. R., & Wiese, W. L. 1988, *Atomic transition probabilities. Scandium through Manganese* (New York: American Institute of Physics (AIP) and American Chemical Society)
- Mashonkina, L., Gehren, T., Shi, J.-R., Korn, A. J., & Grupp, F. 2011, *A&A*, 528, A87
- Maza, N. L., Nieva, M.-F., & Przybilla, N. 2014, *A&A*, 572, A112
- Mermilliod, J. C. 1981a, *A&AS*, 44, 467
- . 1981b, *A&A*, 97, 235
- Michaud, G., Alecian, G., & Richer, J. 2015, *Atomic Diffusion in Stars* (New York: Astronomy and Astrophysics Library, Springer International Publishing), 298

- Miller, M. H., Roig, R. A., & Bengtson, R. D. 1971, *Phys. Rev. A*, 4, 1709
- Moehler, S., Dreizler, S., LeBlanc, F., et al. 2014, *A&A*, 565, A100
- Monier, R. 2005, *A&A*, 442, 563
- Napiwotzki, R., Schoenberger, D., & Wenske, V. 1993, *A&A*, 268, 653
- Netopil, M., & Paunzen, E. 2013, *A&A*, 557, A10
- Nicolet, B. 1981, *A&A*, 104, 185
- Nieva, M. F., & Przybilla, N. 2007, *A&A*, 467, 295
- Nieva, M.-F., & Przybilla, N. 2012, *A&A*, 539, A143
- North, P., & Cramer, N. 1981, in *Liege International Astrophysical Colloquia*, Vol. 23, Liege International Astrophysical Colloquia, 55–59
- O’Brian, T. R., Wickliffe, M. E., Lawler, J. E., Whaling, W., & Brault, J. W. 1991, *Journal of the Optical Society of America B Optical Physics*, 8, 1185
- Pace, G., Danziger, J., Carraro, G., et al. 2010, *A&A*, 515, A28
- Pancino, E., Carrera, R., Rossetti, E., & Gallart, C. 2010, *A&A*, 511, A56
- Paunzen, E., & Netopil, M. 2006, *MNRAS*, 371, 1641
- Paunzen, E., Netopil, M., Iliev, I. K., et al. 2006, *A&A*, 454, 171
- Pedersen, B. B., VandenBerg, D. A., & Irwin, A. W. 1991, in *Lecture Notes in Physics*, Vol. 388, *Challenges to Theories of the Structure of Moderate-Mass Stars*, ed. D. Gough & J. Toomre, Vol. 388 (Berlin: Springer Verlag), 353
- Pickering, J. C., Thorne, A. P., & Perez, R. 2002, *ApJS*, 132, 403

- Pinnington, E. H., Ji, Q., Guo, B., et al. 1993, *Canadian Journal of Physics*, 71, 470
- Piskunov, N. E., Kupka, F., Ryabchikova, T. A., Weiss, W. W., & Jeffery, C. S. 1995, *A&AS*, 112, 525
- Podobedova, L. I., Kelleher, D. E., & Wiese, W. L. 2009, *Journal of Physical and Chemical Reference Data*, 38, 171
- Proffitt, C. R., & Michaud, G. 1991a, *ApJ*, 371, 584
- . 1991b, *ApJ*, 380, 238
- Przybilla, N., Butler, K., Becker, S. R., & Kudritzki, R. P. 2001a, *A&A*, 369, 1009
- Przybilla, N., Butler, K., Becker, S. R., Kudritzki, R. P., & Venn, K. A. 2000, *A&A*, 359, 1085
- Przybilla, N., Butler, K., & Kudritzki, R. P. 2001b, *A&A*, 379, 936
- Przybilla, N., Nieva, M.-F., & Butler, K. 2011, *Journal of Physics Conference Series*, 328, 012015
- Raassen, A. J. J., & Uylings, P. H. M. 1998, *Journal of Physics B Atomic Molecular Physics*, 31, 3137
- Richard, O. 2005, in *EAS Publications Series*, Vol. 17, *Element Stratification in Stars: 40 Years of Atomic Diffusion. Meeting in Honour of Georges Michaud*, held on June 6–10, 2005 in Château de Mons, France, ed. G. Alecian, O. Richard, & S. Vauclair (Les Ulis, France: EDP Sciences), 43–52
- Richard, O., Michaud, G., & Richer, J. 2001, *ApJ*, 558, 377

- Richer, J., & Michaud, G. 2005, in EAS Publications Series, Vol. 17, Element Stratification in Stars: 40 Years of Atomic Diffusion. Meeting in Honour of Georges Michaud, held on June 6–10, 2005 in Château de Mons, France, ed. G. Alecian, O. Richard, & S. Vauclair (Les Ulis, France: EDP Sciences), 53–59
- Richer, J., Michaud, G., Rogers, F., et al. 1998, ApJ, 492, 833
- Richer, J., Michaud, G., & Turcotte, S. 2000, ApJ, 529, 338
- Rogers, F. J., & Iglesias, C. A. 1992, ApJS, 79, 507
- Rohlfs, K., Schrick, K. W., & Stock, J. 1959, ZAp, 47, 15
- Ryabchikova, T. A., Piskunov, N. E., Kupka, F., & Weiss, W. W. 1997, Baltic Astronomy, 6, 244
- Ryabchikova, T. A., & Smirnov, Y. M. 1989
- Santrich, O. J. K., Pereira, C. B., & Drake, N. A. 2013, A&A, 554, A2
- Sbordone, L. 2005, Memorie della Societa Astronomica Italiana Supplementi, 8, 61
- Sbordone, L., Bonifacio, P., Castelli, F., & Kurucz, R. L. 2004, Memorie della Societa Astronomica Italiana Supplementi, 5, 93
- Schneider, H. 1985, A&AS, 61, 45
- Schultz, G. V., & Wiemer, W. 1975, A&A, 43, 133
- Shamey, L. J. 1969, PhD thesis, UNIVERSITY OF COLORADO AT BOULDER.
- Sigut, T. A. A., & Landstreet, J. D. 1990, MNRAS, 247, 611

- Sitnova, T., Mashonkina, L., Ryabchikova, T., & Pakhomov, Y. 2014, in *Putting A Stars into Context: Evolution, Environment, and Related Stars*, ed. G. Mathys, E. R. Griffin, O. Kochukhov, R. Monier, & G. M. Wahlgren, 151–156
- Smalley, B. 2004, in *IAU Symposium, Vol. 224, The A-Star Puzzle*, ed. J. Zverko, J. Ziznovsky, S. J. Adelman, & W. W. Weiss, 131–138
- Steffen, M. 1985, *A&AS*, 59, 403
- Strobel, A., Skaba, W., & Proga, D. 1992, *A&AS*, 93, 271
- Stütz, C., Bagnulo, S., Jehin, E., et al. 2006, *A&A*, 451, 285
- Talbert, F. D. 1965, *PASP*, 77, 19
- Talon, S., Richard, O., & Michaud, G. 2006, *ApJ*, 645, 634
- Theodosiou, C. E. 1989, *Phys. Rev. A*, 39, 4880
- Turcotte, S., Richer, J., & Michaud, G. 1998a, *ApJ*, 504, 559
- Turcotte, S., Richer, J., Michaud, G., Iglesias, C. A., & Rogers, F. J. 1998b, *ApJ*, 504, 539
- van den Bergh, S., & Hagen, G. L. 1975, *AJ*, 80, 11
- Varenne, O., & Monier, R. 1999, *A&A*, 351, 247
- Vick, M., Michaud, G., Richer, J., & Richard, O. 2010, *A&A*, 521, A62
- Vidal, C. R., Cooper, J., & Smith, E. W. 1973, *ApJS*, 25, 37
- Villanova, S., Carraro, G., & Saviane, I. 2009, *A&A*, 504, 845
- Vleeming, G. 1974, *A&AS*, 16, 331
- Wedemeyer, S. 2001, *A&A*, 373, 998

- Wickliffe, M. E., & Lawler, J. E. 1997, *ApJS*, 110, 163
- Wiese, W. L., & Fuhr, J. R. 2009, *Journal of Physical and Chemical Reference Data*, 38, 565
- Wiese, W. L., Fuhr, J. R., & Deters, T. M., eds. 1996, *Atomic transition probabilities of carbon, nitrogen, and oxygen : a critical data compilation* (Washington, DC: American Chemical Society)
- Wiese, W. L., & Martin, G. A. 1980, *Wavelengths and transition probabilities for atoms and atomic ions: Part 2. Transition probabilities*, NSRDS-NBS Vol. 68. (NSRDS-NBS, US Department of Commerce, National Bureau of Standards)
- Wiese, W. L., Smith, M. W., & Miles, B. M. 1969, *Atomic transition probabilities. Vol. 2: Sodium through Calcium. A critical data compilation* (Washington, D.C.: NSRDS-NBS, US Department of Commerce, National Bureau of Standards)
- Zacharias, N., Urban, S. E., Zacharias, M. I., et al. 2004, *AJ*, 127, 3043
- Zahn, J.-P. 2005, in *EAS Publications Series*, Vol. 17, *Element Stratification in Stars: 40 Years of Atomic Diffusion. Meeting in Honour of Georges Michaud, held on June 6–10, 2005 in Château de Mons, France*, ed. G. Alecian, O. Richard, & S. Vauclair (Les Ulis, France: EDP Sciences), 157–166

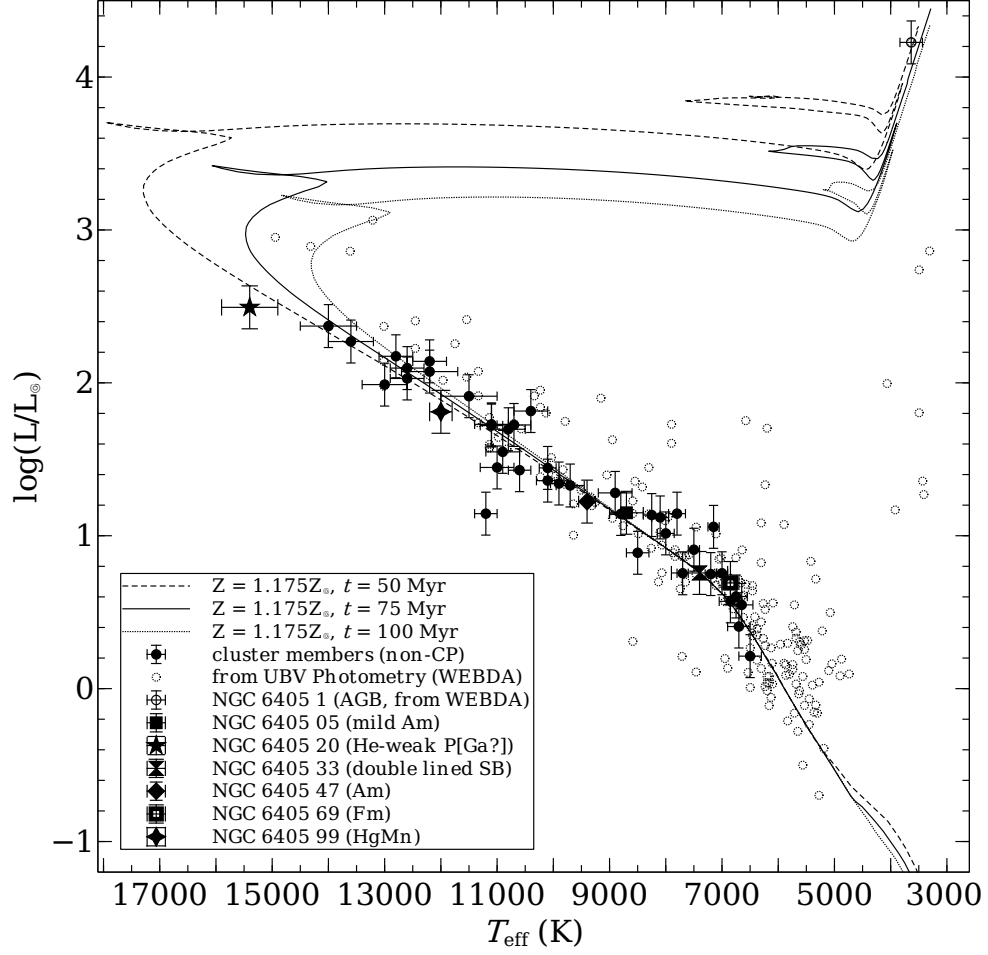


Fig. 1.— HR diagram of the observed stars.

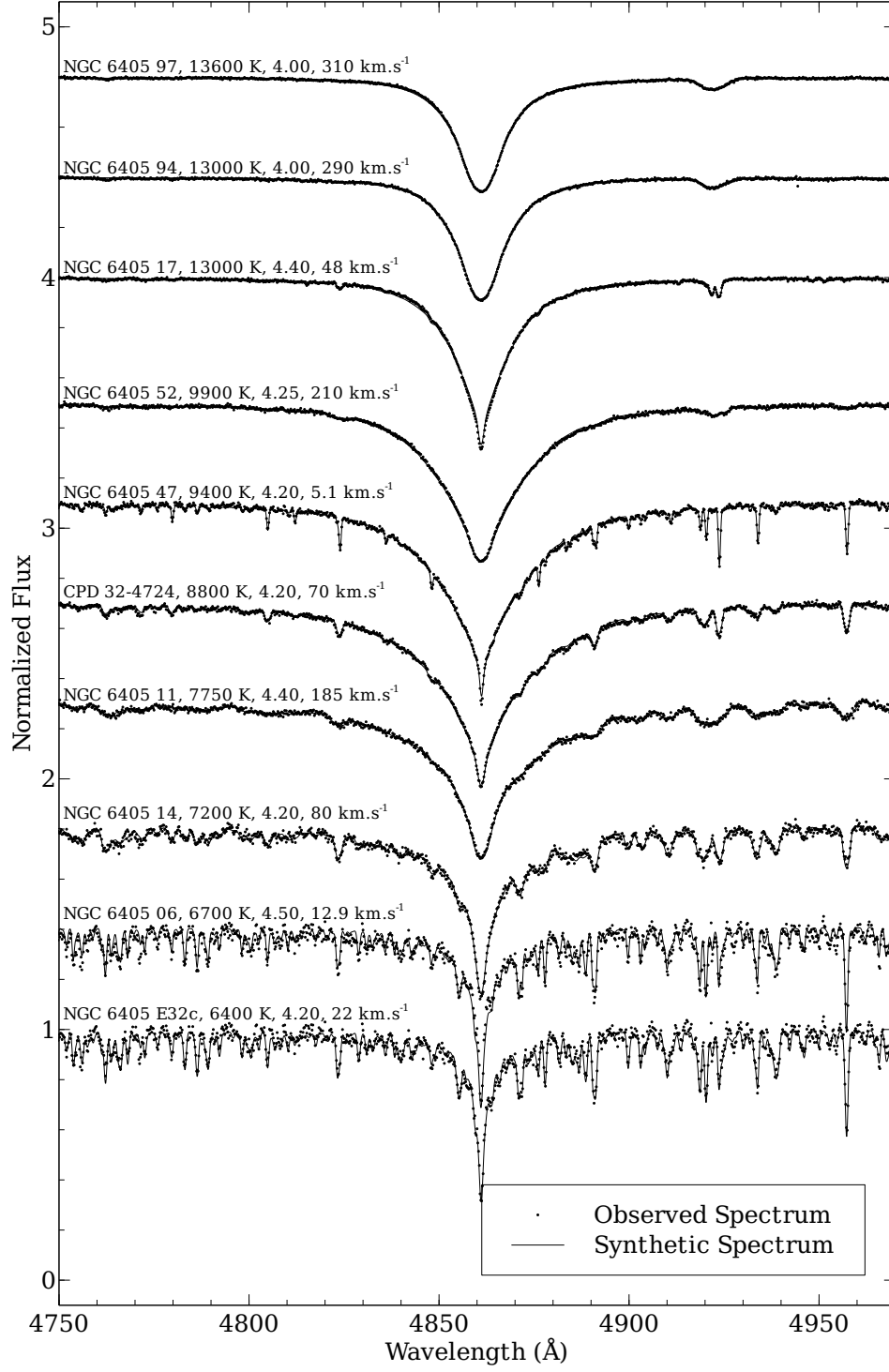


Fig. 2.— Gallery of the H_β region from the late B stars to the F stars

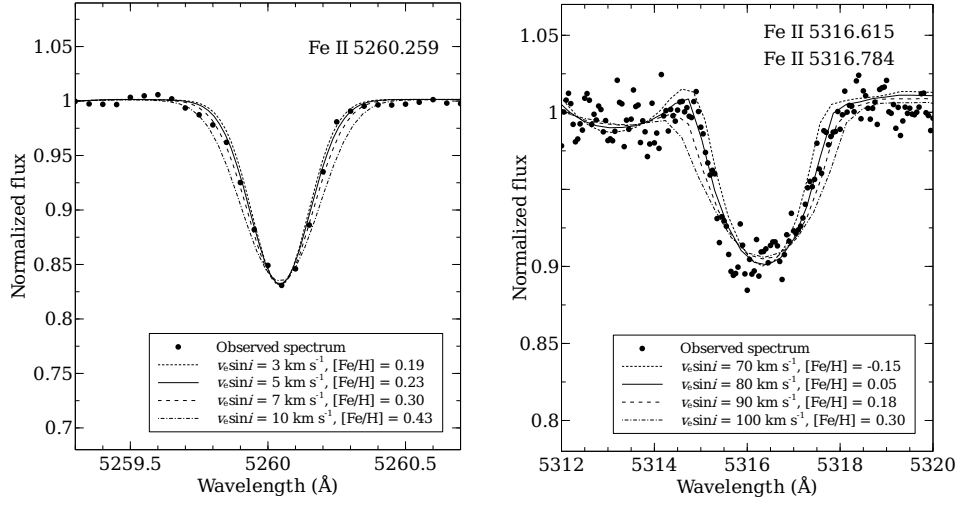


Fig. 3.— $v_e \sin i$ determination by adjusting the synthetic spectra for the stars CD-32 13109 (left panel) and GSC07380-00766 (right panel).

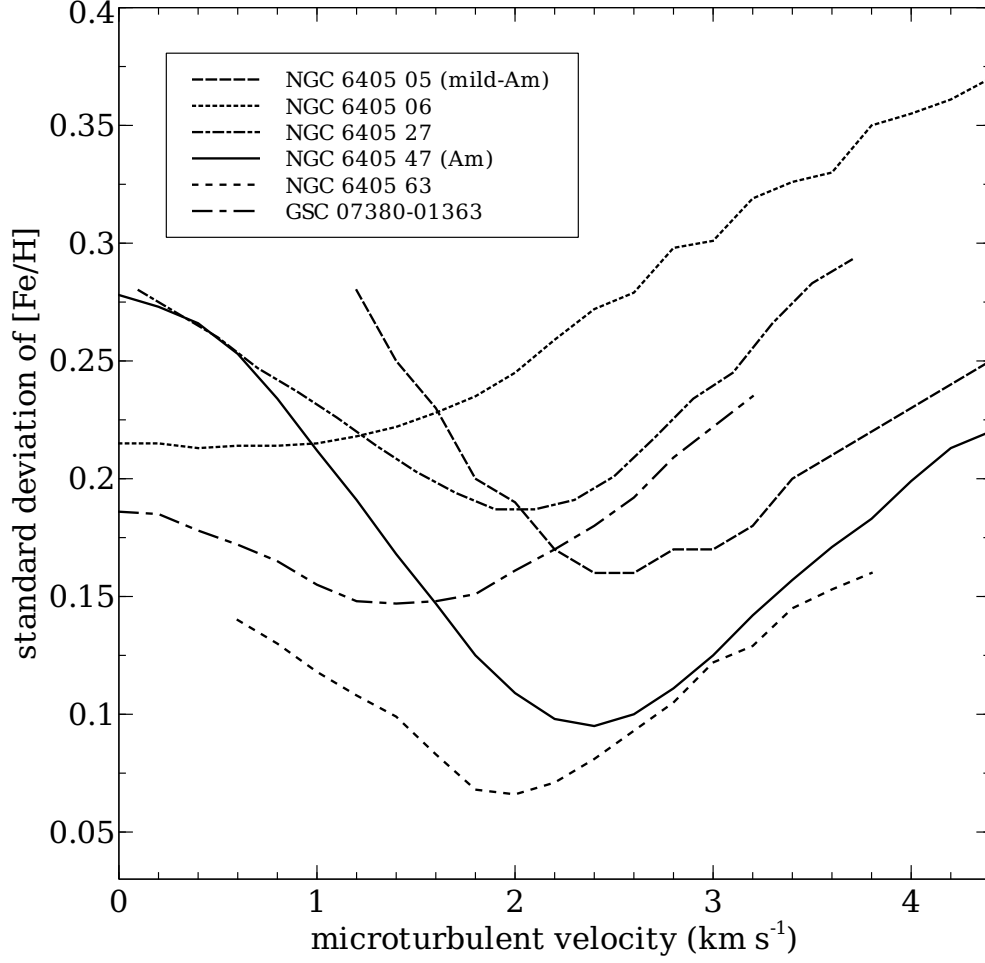


Fig. 4.— Microturbulence determination by minimizing the standard deviation of [Fe/H].

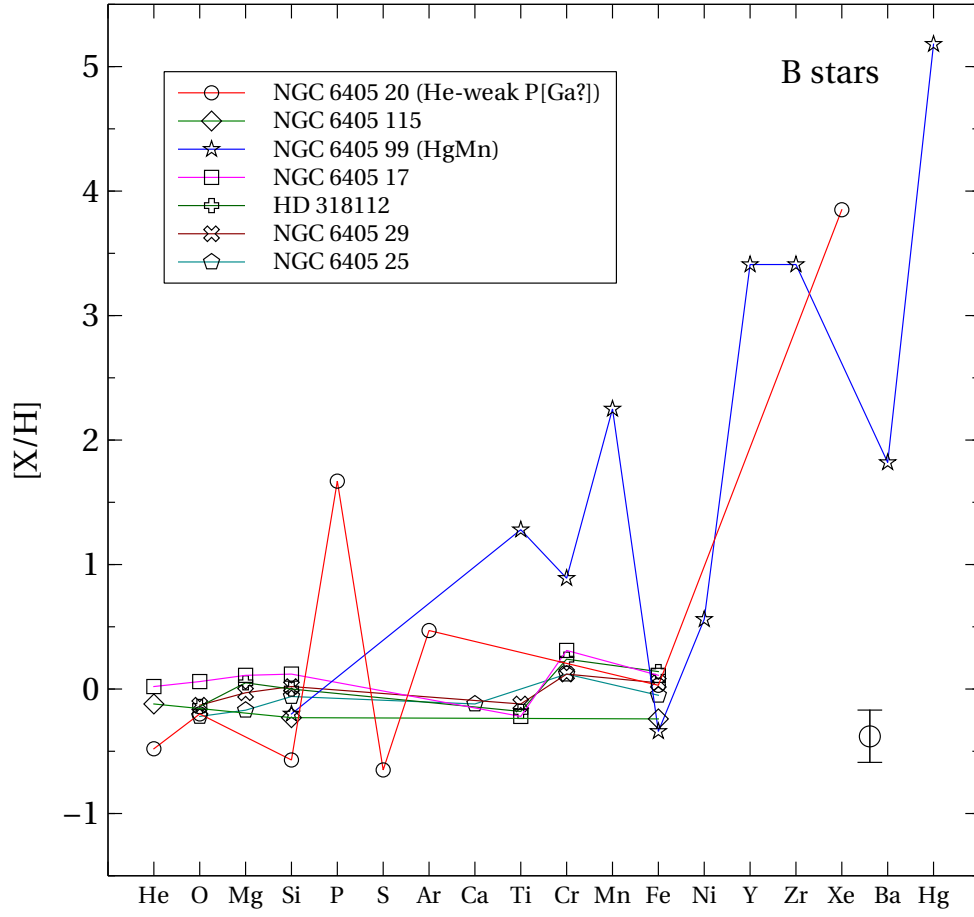


Fig. 5.— Abundance pattern of B-type cluster members (deviations from solar abundances in Grevesse & Sauval (1998))

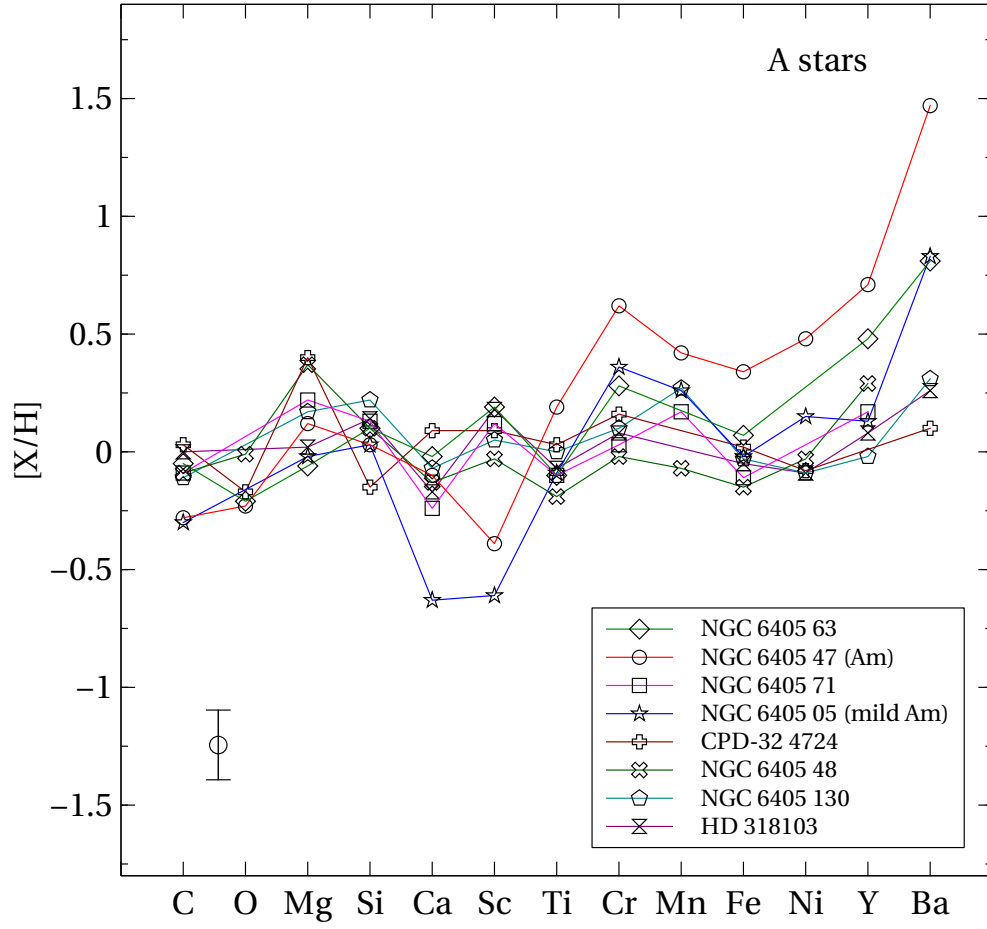


Fig. 6.— Abundance pattern of A-type cluster members (deviations from solar abundances in Grevesse & Sauval (1998))

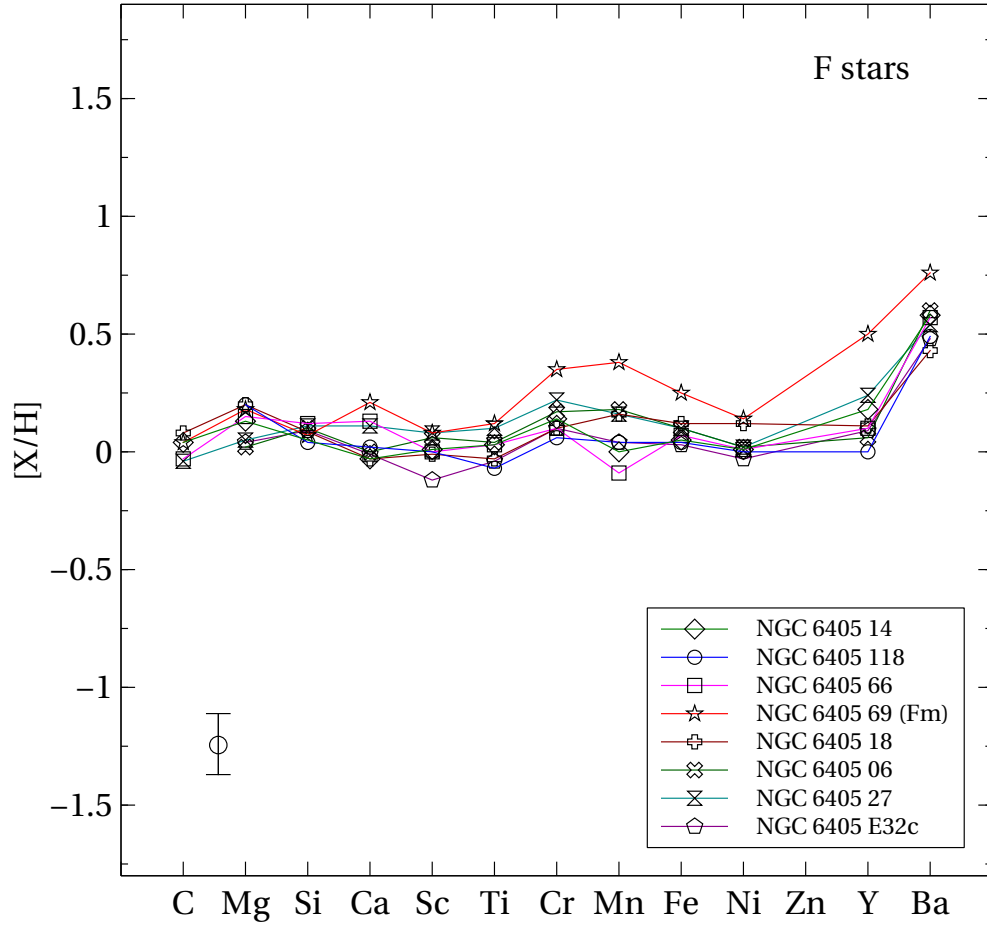


Fig. 7.— Abundance pattern of F-type cluster members (deviations from solar abundances in Grevesse & Sauval (1998))

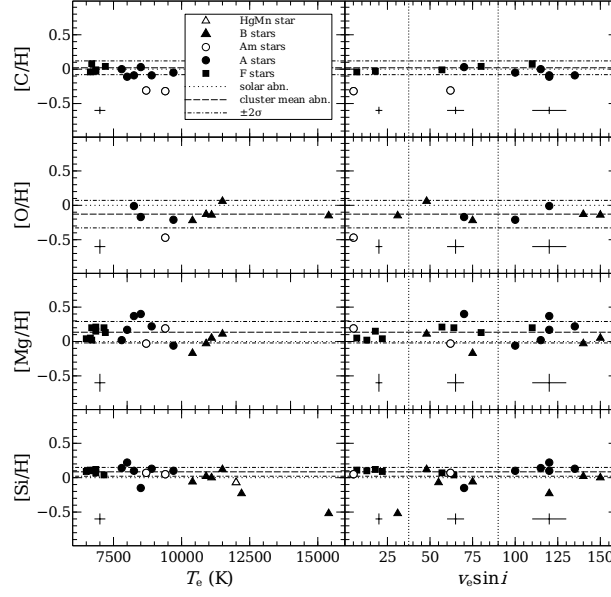


Fig. 8.— Abundances of C, O, Mg, and Si relative to the Sun (Grevesse & Sauval 1998) versus T_{eff} and $v_e \sin i$.

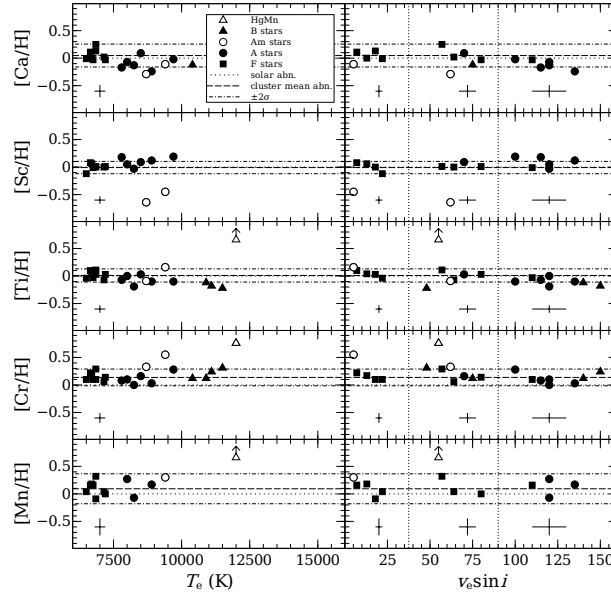


Fig. 9.— Same as in Fig. 8 but for Ca, Sc, Cr, Ti, and Mn.

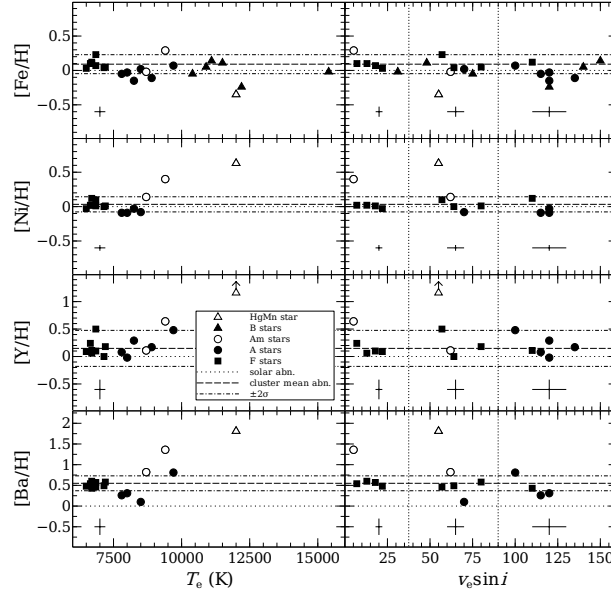


Fig. 10.— Same as in Fig. 8 but for Fe, Ni, Ba, Y.

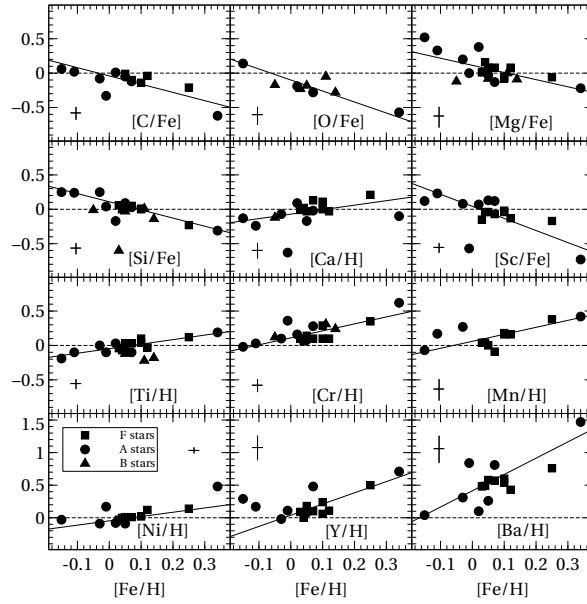


Fig. 11.— Abundances of the elements relative to the Sun (Grevesse & Sauval 1998) versus iron abundance.

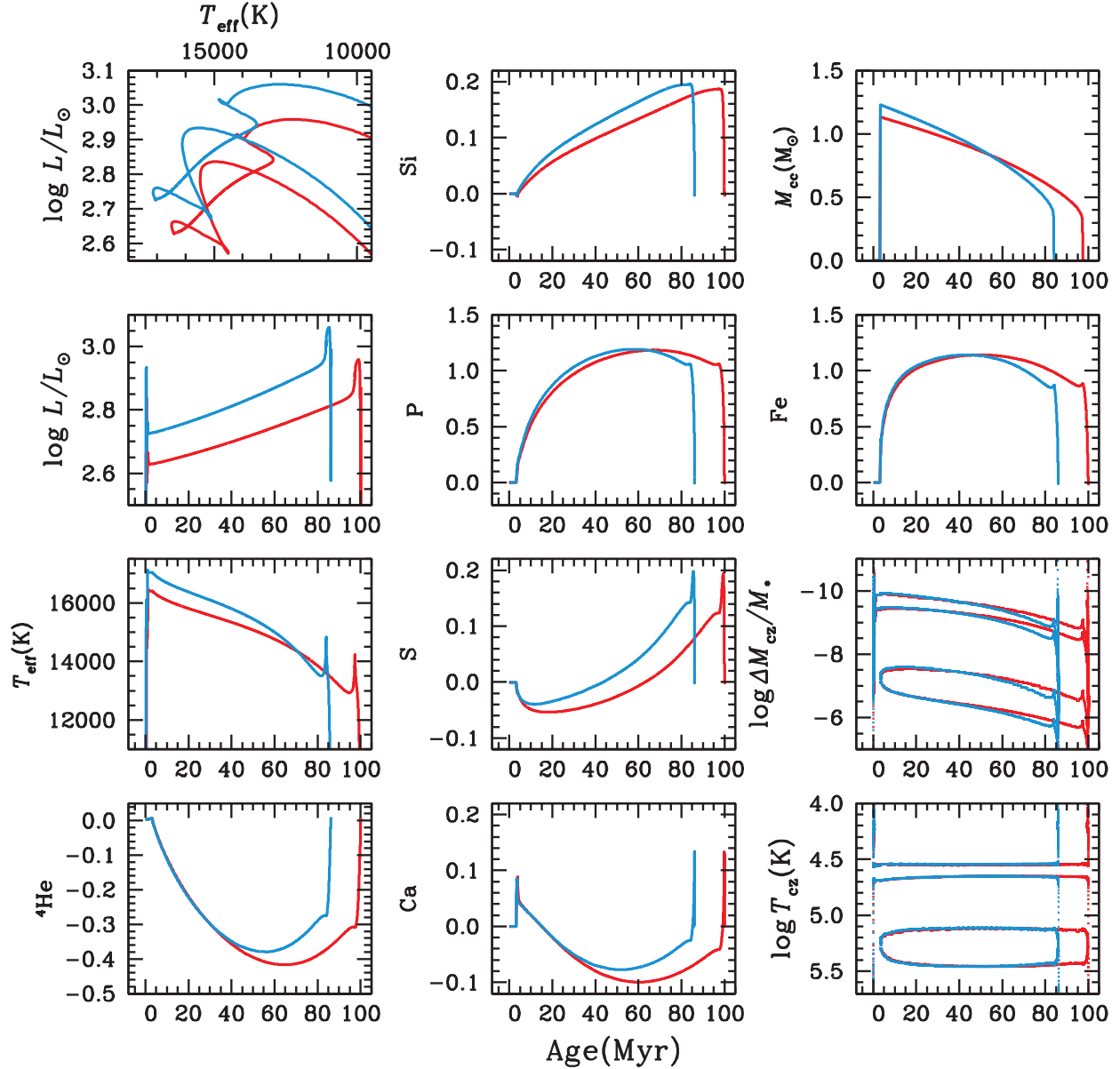


Fig. 12.— Evolution of properties of two models for HD 318101, with $M_* = 4.7$ (red) and 5.0 M $_{\odot}$ (blue). The initial metallicity $Z_0 = 0.02$. Surface layers are homogenized down to the bottom of the HeII convection zone. Extra turbulence T150KD1K-3 is added (see text), covering mostly the interior of the Mn-Fe-Ni convection zone; the red curves correspond to the T150K model of figure 15. ΔM_{cz} is mass measured from the star surface. Panels for chemical elements show mass fraction changes $\log_{10}(X/X_0)_{\text{element}}$ at the surface.

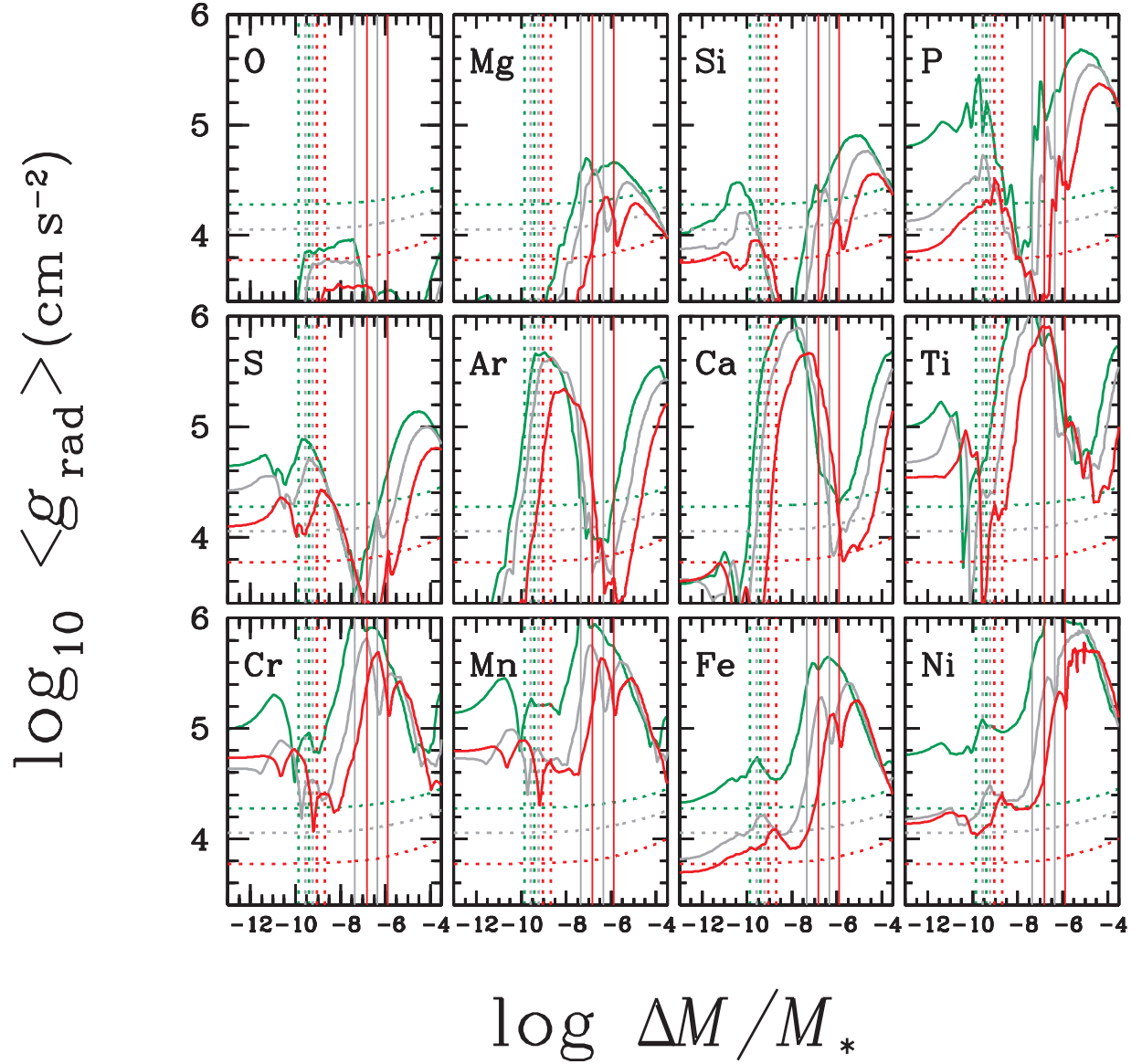


Fig. 13.— Radiative acceleration profiles from XEVOL for a number of elements in the 4.7 M_{\odot} model T150KD1K-3. Profiles are shown for ages 2 Myr (green), 50 Myr (grey), and 85 Myr (red). The horizontal dotted curves show the run of $\log g$ through the envelope, while vertical lines show the limits of envelope convection zones, for He II (dotted) and iron-group elements (solid, if present).

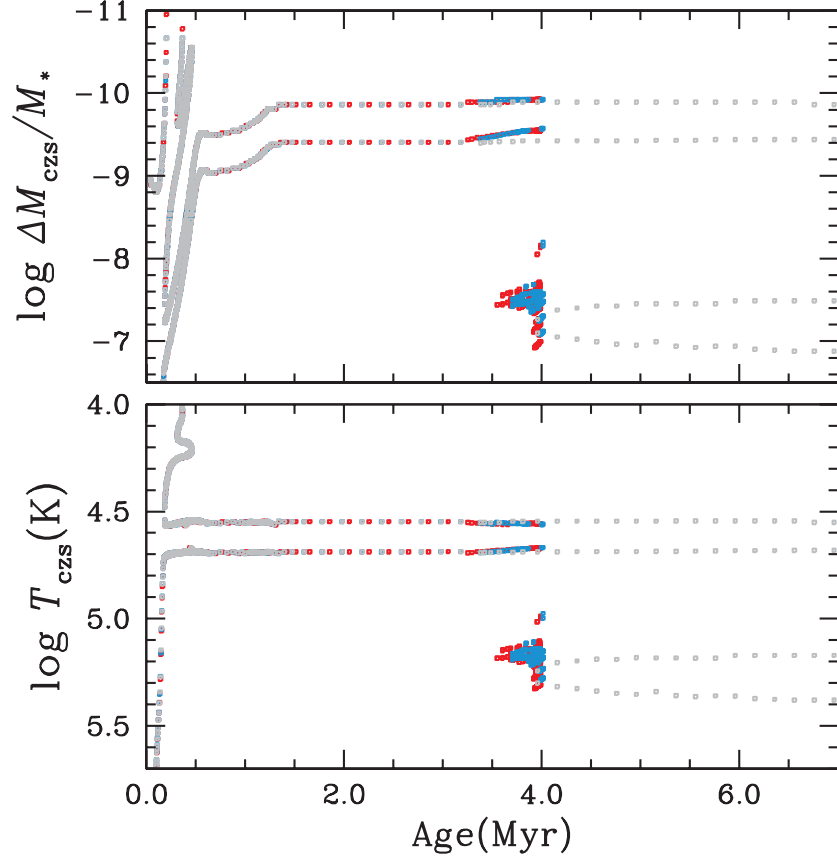


Fig. 14.— Envelope convection zone boundaries in an evolving $4.7 M_{\odot}$ star with initial metallicity $Z_0 = 0.02$ and the same initial *metal proportions* as in the best XEVOL age zero solar model. The figure shows the boundaries for every converged model in the time sequences. Three models are shown (see text for details): T65KD10-4 (blue), with weak, short range turbulence below the HeII convection zone; T150KD1K-3 (grey), with much stronger turbulence in the iron convection zone only (grey); T65KD30-4W5E-15 (red), with turbulence 3 times the strength of that in the blue model, plus weak, constant stellar mass loss ($5 \times 10^{-15} M_{\odot}/\text{yr}$). Homogeneity is artificially enforced in layers cooler than 65 000 K ($\log T \lesssim 4.8$).

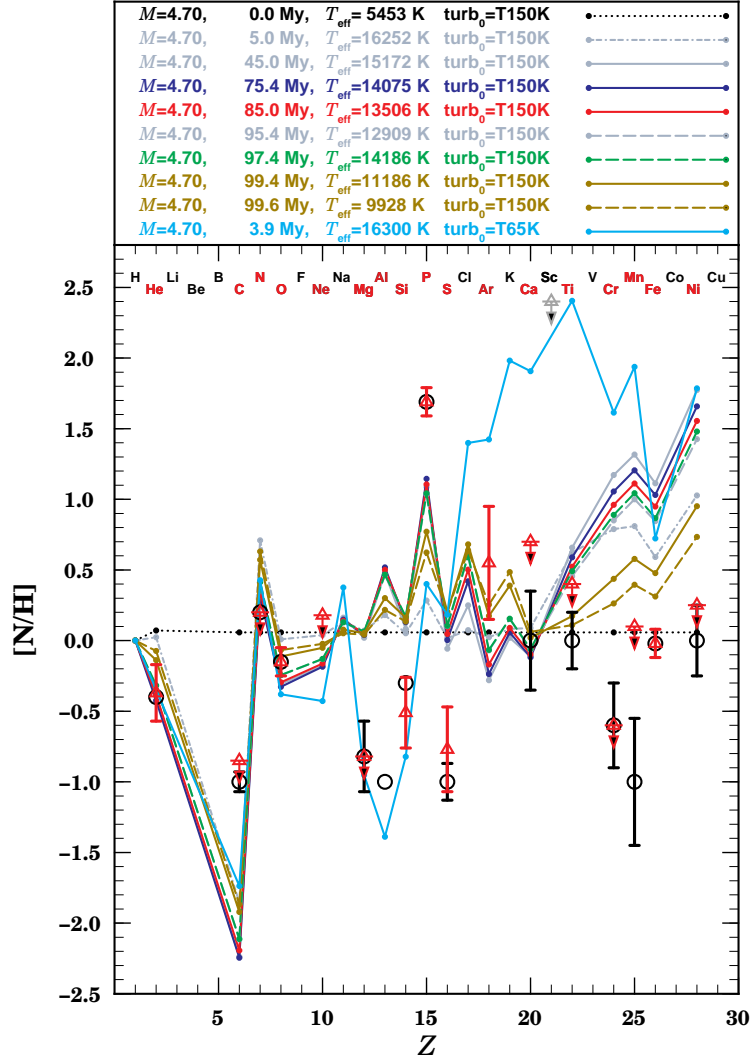


Fig. 15.— Evolution of computed surface abundance patterns in XEVOL models T150KD1K-3 (first nine profiles) and T65KD10-4 (last profile), for star HD 318101, with $M_* = 4.7 M_\odot$. The top legend indicates the age, effective temperature and level of turbulence of each model. Observations from R. Monier (*black circles*, private communication) and Kılıçoğlu et al (*red triangles*, present paper) are shown for comparison. Scandium, measured but not included in the simulations, is shown as a *grey triangle*. Lines for ages > 99 Myr correspond to the end of the main-sequence and the rapid wiping-out of anomalies. Elements for which there are both measurements and modeled values appear in red at the top of the plot. Abundances are relative to the Sun.

Table 1. Age, distance, color excess and metallicity of M6

Reference	Age (Myr/log t [s])	Distance (pc)	Color Excess $E(B - V)$	Metallicity [Fe/H]
Rohlfis et al. (1959)	100 / 8.00	630 ± 50	0.156	...
Becker (1961)	...	505	0.1	...
Eggen (1961) ^a	...	501	0.13	...
Johnson et al. (1961)	...	630 ± 90^b	0.16	...
Talbert (1965)	...	480 ± 40
Lindoff (1968)	50 / 7.70
Becker & Fenkart (1971)	...	445	0.17	...
Vleeming (1974)	100 / 8.00	450 ± 50	0.15	...
Harris (1976)	$52.5 / 7.72 \pm 0.10$
Mermilliod (1981a)	...	460	0.15	...
Mermilliod (1981b)	51.3 / 7.71
North & Cramer (1981)	79.4 / 7.9	...	0.16 ^c	...
Cameron (1985b)	0.09 ± 0.02	0.07
Jura (1987)	...	600
Strobel et al. (1992)	130 / 8.1	457 ^d	0.15	...
Dias et al. (2002)	94 / 7.974	487	0.144	0.06
Paunzen et al. (2006)	100 / 8.00	450 ± 70	0.20 ± 0.05	...
Paunzen & Netopil (2006)	$71 \pm 21 / 7.85$	473 ± 16	0.14 ± 0.02	...
Ahumada & Lapasset (2007)	93 / 7.97	...	0.14	...
Landstreet et al. (2007)	$63 / 7.8 \pm 0.15$
Kharchenko et al. (2009)	81 / 7.91	487	0.14	...
Francis & Anderson (2012)	...	322 ± 32
Netopil & Paunzen (2013)	79.4 / 7.90	...	0.17 ± 0.02	0.09 ± 0.11
Average with standard dev.	82 ± 23	490 ± 80	0.15 ± 0.03	0.07
This study	$80 \pm 20 / 7.90$	400 ± 50	...	0.07 ± 0.03

^areported via Antalová (1972)

^berror adopted from the uncertainties of their given distance modulus

^ccoverted value from $E(B_2 - V_1) = 0.135$ (see Section 3.2.1)

^dvalue calculated from their given their given distance modulus (8.3 mag)

Table 2. Observation log

Date	Setting	MJD (start of exp. time)	Exposure time (s)
30.05.2007	H09B	54250.34380149	410
		54250.34941879	410
		54250.35476998	410
05.06.2007	H09B	54256.12558588	410
		54256.13093846	410
		54256.13629534	410
	H11	54256.14208523	290
		54256.14605750	290
		54256.15002295	290
	LR3	54256.15521383	120
		54256.15721080	120

Table 3. List of selected targets

Star	Rohlf's et	V	Membership probability		Radial velocity (v_{rad})		HR	S/N
	al. (1959) id. no.		D2006 (per cent)	FM2008 (per cent)	FM2008 (km s^{-1})	This study (km s^{-1})	Diagram criterion	
HD 160093	33	11.29	...	97.1	39.23 ± 2.58	(SB2)	Yes	221/156/123
HD 160167	115	8.56	61	1.1	-1.53 ± 5.94	-8.21 ± 3.07	Yes	482/447/396
HD 160188	...	9.31	-4.34 ± 2.80	Yes	319/400/355
HD 160222	97	8.50	52	6.76 ± 18.18	Yes	478/616/516
HD 160259	28	8.73	4	4.4	-71.71 ± 5.09	0.02 ± 6.17	Yes	427/510/401
HD 160260	70	8.32	61	-14.38 ± 9.44	Yes	573/686/539
HD 160297	41	8.84	39	-5.11 ± 2.59	No	479/512/403
HD 160298	94	8.60	3	10.4	-65.24 ± 5.68	-10.51 ± 1.70	Yes	522/564/444
HD 160392	17	9.00	...	62.5	-2.59 ± 4.70	-8.86 ± 1.03	Yes	545/570/387
HD 318091	5	10.37	-4.21 ± 1.26	Yes	154/263/210
HD 318092	22	9.40	18	89.3	55.26 ± 7.76	-13.14 ± 7.61	Yes	403/435/342
HD 318093	25	9.02	18	57.5	-24.73 ± 4.63	-6.76 ± 1.68	No	385/518/385
HD 318094	42	10.40	48	-6.88 ± 2.02	Yes	237/351/201
HD 318099	29	9.79	30	-7.48 ± 2.47	Yes	224/353/278
HD 318101	20	8.26	32	95.6	-10.76 ± 4.93	-8.13 ± 0.78	...	450/527/373
HD 318103	...	10.32	-7.46 ± 4.60	No	214/374/227
HD 318110	96	8.92	54	-7.78 ± 6.27	Yes	653/452/452
HD 318111	...	9.40	62	75.2	-13.62 ± 6.08	-10.68 ± 4.23	Yes	468/539/341
HD 318112	...	9.38	63	-10.36 ± 3.55	Yes	427/571/344
HD 318113	95	10.07	55	-5.98 ± 4.42	No	270/308/243
HD 318114	64	10.10	54	-7.73 ± 4.08	Yes	237/212/236
HD 318117	37	8.75	24	-11.04 ± 2.38	Yes	478/547/430
HD 318118	63	10.10	38	-7.16 ± 2.11	Yes	222/356/238
HD 318126	99	9.35	41	(var.)	Yes	360/479/423
CD-32 13092	73	10.03	56	-4.64 ± 3.52	Yes	255/344/260
CD-32 13093	52	10.11	63	-9.53 ± 4.91	Yes	205/218/234
CD-32 13097	51	9.89	41	-5.06 ± 5.94	Yes	254/295/256
CD-32 13106	71	10.08	62	-3.28 ± 3.51	Yes	217/333/239
CD-32 13109	47	10.30	56	-2.45 ± 0.87	Yes	153/277/184
CD-32 13126	44	10.39	61	-3.41 ± 3.84	Yes	150/256/197

Table 3—Continued

Star	Rohlf's et al. (1959) id. no.	V	Membership probability		Radial velocity (v_{rad})		HR Diagram criterion	S/N
			D2006 (per cent)	FM2008 (per cent)	FM2008 (km s $^{-1}$)	This study (km s $^{-1}$)		
CD-32 13148	130	10.64	59	-6.15 \pm 3.75	Yes	102/170/142
CPD-32 4693	118	10.54	32	-6.73 \pm 1.67	No	100/217/211
CPD-32 4713	48	10.36	54	-4.97 \pm 3.11	Yes	274/252/199
CPD-32 4724	...	11.00	49	-8.83 \pm 1.69	Yes	292/322/274
CPD-32 4739	67	10.91	48	-9.05 \pm 3.74	Yes	188/241/203
GSC 7380-0206	18	11.70	57	-10.09 \pm 3.30	Yes	134/85/119
GSC 7380-0281	26	11.31	58	-7.96 \pm 4.66	Yes	141/145/132
GSC 7380-0339	27	11.84	0	-9.27 \pm 0.54	Yes	45/78/51
GSC 7380-0539	31	11.30	45	-2.84 \pm 3.04	Yes	54/170/134
GSC 7380-0766	14	11.31	48	-10.57 \pm 2.23	Yes	219/137/102
GSC 7380-0986	66	11.77	45	-9.63 \pm 0.62	Yes	98/154/91
GSC 7380-1170	6	12.19	25	-9.00 \pm 0.23	Yes	56/120/99
GSC 7380-1211	69	11.47	39	-7.21 \pm 1.16	Yes	62/146/115
GSC 7380-1363	...	12.69	41	-8.33 \pm 0.85	Yes	34/120/59
Weighted mean of radial velocity =						-8.48 \pm 0.17		

Table 4. $\log L/L_\odot$, $\log T_{\text{eff}}$, M/M_\odot and fractional age (τ) for the members

Star	Id no.	$\log L/L_\odot$	$\log T_{\text{eff}}$	M/M_\odot	τ
HD 160167	115	2.14	4.086	3.12 ± 0.22	0.29 ± 0.05
HD 160188	...	1.72	4.029	2.53 ± 0.19	0.17 ± 0.03
HD 160222	97	2.27	4.134	3.64 ± 0.31	0.43 ± 0.09
HD 160259	28	2.07	4.086	3.13 ± 0.31	0.29 ± 0.08
HD 160260	70	2.37	4.146	3.83 ± 0.38	0.48 ± 0.12
HD 160297	41	1.14	4.049	2.57 ± 0.13	0.17 ± 0.02
HD 160298	94	2.17	4.107	3.33 ± 0.23	0.34 ± 0.06
HD 160392	17	1.91	4.061	2.86 ± 0.30	0.23 ± 0.06
HD 318091	5	1.15	3.940	1.88 ± 0.16	0.08 ± 0.02
HD 318092	22	1.72	4.041	2.63 ± 0.13	0.18 ± 0.02
HD 318093	25	1.82	4.017	2.47 ± 0.18	0.16 ± 0.03
HD 318095	42	1.14	3.944	1.89 ± 0.10	0.08 ± 0.01
HD 318099	29	1.55	4.037	2.53 ± 0.19	0.17 ± 0.03
HD 318101	20	2.49	4.188	4.33 ± 0.43	0.65 ± 0.17
HD 318103	...	1.14	3.892	1.67 ± 0.07	0.06 ± 0.01
HD 318110	96	2.03	4.100	3.21 ± 0.23	0.31 ± 0.05
HD 318111	...	1.7	4.033	2.54 ± 0.19	0.17 ± 0.03
HD 318112	...	1.73	4.045	2.64 ± 0.20	0.18 ± 0.04
HD 318113	95	1.45	4.041	2.53 ± 0.19	0.17 ± 0.03
HD 318114	64	1.36	4.004	2.27 ± 0.12	0.13 ± 0.02
HD 318117	37	2.1	4.100	3.23 ± 0.22	0.31 ± 0.05
HD 318118	63	1.33	3.987	2.45 ± 0.14	0.11 ± 0.02
HD 318126	99	1.81	4.079	2.96 ± 0.16	0.25 ± 0.04
CD-32 13092	73	1.43	4.025	2.43 ± 0.13	0.15 ± 0.02
CD-32 13093	52	1.34	3.996	2.21 ± 0.09	0.12 ± 0.01
CD-32 13097	51	1.44	4.004	2.28 ± 0.09	0.13 ± 0.01
CD-32 13106	71	1.28	3.949	1.95 ± 0.15	0.08 ± 0.02
CD-32 13109	47	1.22	3.973	2.05 ± 0.09	0.10 ± 0.01
CD-32 13126	44	1.12	3.908	1.73 ± 0.07	0.06 ± 0.01
CD-32 13148	130	1.02	3.903	1.70 ± 0.07	0.06 ± 0.01
CPD-32 4693	118	1.06	3.854	1.51 ± 0.05	0.04 ± 0.01
CPD-32 4713	48	1.14	3.916	1.77 ± 0.07	0.06 ± 0.01

Table 4—Continued

Star	Id no.	$\log L/L_{\odot}$	$\log T_{\text{eff}}$	M/M_{\odot}	τ
CPD-32 4724	...	0.89	3.929	1.80 ± 0.09	0.07 ± 0.01
CPD-32 4739	67	0.91	3.875	1.59 ± 0.04	0.05 ± 0.01
GSC 7380-0206	18	0.6	3.829	1.39 ± 0.09	0.03 ± 0.01
GSC 7380-0281	26	0.75	3.845	1.46 ± 0.06	0.04 ± 0.01
GSC 7380-0339	27	0.55	3.823	1.36 ± 0.10	0.03 ± 0.01
GSC 7380-0539	31	0.75	3.886	1.63 ± 0.05	0.05 ± 0.01
GSC 7380-0766	14	0.75	3.857	1.51 ± 0.05	0.04 ± 0.01
GSC 7380-0986	66	0.57	3.836	1.41 ± 0.11	0.03 ± 0.01
GSC 7380-1170	6	0.41	3.826	1.34 ± 0.11	0.03 ± 0.01
GSC 7380-1211	69	0.69	3.836	1.42 ± 0.08	0.03 ± 0.01
GSC 7380-1363	...	0.21	3.813	1.24 ± 0.10	0.02 ± 0.01

Table 5. Fundamental parameters for the programme stars

Star	Rohlf's et	Photometric		Final		v_{mic}	$v_{\text{e}} \sin i$ (km s ^{−1})	Sp. T.
	al. (1959) id. no	T_{eff} (K)	log g (dex)	T_{eff} (K)	log g (dex)			
HD 160093	33	6892	4.35	7400 ± 500	...	(spectroscopic binary)		...
HD 160167	115	13032	4.19	12200 ± 300	4.00 ± 0.10	0	120 ± 10	B8
HD 160188	...	(12632)	...	10700 ± 300	4.10 ± 0.10	0	300 ± 20	B9
HD 160222	97	13433	4.03	13600 ± 400	4.00 ± 0.15	0	310 ± 20	B7
HD 160259	28	11793	4.35	12200 ± 500	4.15 ± 0.10	0	240 ± 20	B8
HD 160260	70	13967	3.99	14000 ± 500	4.10 ± 0.10	0	250 ± 25	B6
HD 160297	41	11200	4.20	11200 ± 200	4.20 ± 0.10	0	280 ± 20	B9
HD 160298	94	12961	4.04	12800 ± 300	4.00 ± 0.10	0	290 ± 20	B7
HD 160392	17	12090	4.19	11500 ± 500	4.10 ± 0.10	0	48 ± 3	B8
HD 318091	5	9079	4.21	8700 ± 300	4.00 ± 0.10	2.5	62 ± 5	A3m
HD 318092	22	11185	3.95	11100 ± 200	4.10 ± 0.10	0	280 ± 20	B9
HD 318093	25	10368	4.13	10400 ± 300	4.30 ± 0.15	0	75 ± 5	B9
HD 318094	42	8951	4.28	8800 ± 200	4.10 ± 0.15	2	170 ± 15	A3
HD 318099	29	11199	4.21	10900 ± 300	4.30 ± 0.10	0	140 ± 10	B9
HD 318101	20	15864	4.04	15400 ± 300	4.00 ± 0.10	0	31 ± 3	B5
HD 318103	...	(7470)	...	7800 ± 150	4.20 ± 0.50	2.1	115 ± 5	A7
HD 318110	96	12798	4.10	12600 ± 300	4.10 ± 0.15	0	210 ± 15	B7
HD 318111	...	(10911)	...	10800 ± 300	4.00 ± 0.10	0	260 ± 20	B9
HD 318112	...	(11521)	...	11100 ± 300	4.20 ± 0.10	0	150 ± 10	B9
HD 318113	95	9881	4.33	11000 ± 300	4.60 ± 0.10	0	165 ± 15	B9
HD 318114	64	9674	4.19	10100 ± 200	4.30 ± 0.10	2	220 ± 20	A0
HD 318117	37	12776	4.12	12600 ± 300	4.10 ± 0.10	0	220 ± 20	B7
HD 318118	63	10116	4.27	9700 ± 250	4.20 ± 0.15	2	100 ± 5	A0
HD 318126	99	12369	4.33	12000 ± 200	4.10 ± 0.10	0.5	55 ± 5	B8
CD-32 13092	73	9965	4.16	10600 ± 200	4.30 ± 0.10	0	280 ± 25	B9
CD-32 13093	52	9860	4.25	9900 ± 150	4.25 ± 0.10	1.9	210 ± 10	A0
CD-32 13097	51	9925	4.22	10100 ± 150	4.20 ± 0.10	1.9	240 ± 10	A0
CD-32 13106	71	9418	4.14	8900 ± 300	4.00 ± 0.15	2	135 ± 15	A2
CD-32 13109	47	9396	4.30	9400 ± 150	4.20 ± 0.10	2.4	5.1 ± 0.8	A1m
CD-32 13126	44	8465	4.01	8100 ± 150	3.80 ± 0.15	1.6	270 ± 25	A5

Table 5—Continued

Star	Rohlfs et	Photometric		Final		v_{mic}	$v_e \sin i$	Sp. T.
	al. (1959)	T_{eff}	$\log g$	T_{eff}	$\log g$			
	id. no	(K)	(dex)	(K)	(dex)	(km s ⁻¹)		
CD-32 13148	130	8079	3.94	8000 ± 150	4.10 ± 0.30	2.4	120 ± 10	A6
CPD-32 4693	118	7044	4.60	7150 ± 100	4.10 ± 0.30	2.4	64 ± 5	F1
CPD-32 4713	48	8387	4.07	8250 ± 150	4.05 ± 0.10	2.5	120 ± 10	A5
CPD-32 4724	8500 ± 200	4.20 ± 0.20	2.7	70 ± 5	A4
CPD-32 4739	67	7449	4.29	7500 ± 100	4.00 ± 0.20	2.3	180 ± 10	A9
GSC07380-00206	18	6045	3.22	6750 ± 200	4.00 ± 0.4	1.9	110 ± 10	F3
GSC07380-00281	26	6680	4.10	7000 ± 100	4.10 ± 0.30	2.5	210 ± 15	F2
GSC07380-00339	27	(6147)	...	6650 ± 200	(4.80)	2	7 ± 1	F5
GSC07380-00539	31	(9359)	...	7700 ± 100	3.50 ± 0.40	2.5	65 ± 5	A7
GSC07380-00766	14	7230	4.76	7200 ± 100	4.20 ± 0.30	2.2	80 ± 5	F1
GSC07380-00986	66	6532	4.45	6850 ± 200	(4.40)	2	17.9 ± 0.5	F2
GSC 07380-01170	6	(6312)	...	6700 ± 200	(4.50)	1	12.9 ± 0.8	F3
GSC07380-01211	69	6382	3.81	6850 ± 150	(4.40)	2.2	57 ± 3	F3
GSC07380-01363	E32c	(6279)	...	6500 ± 200	(4.20)	1.5	22 ± 1	F6

^aThe star IDs are listed in columns 1 and 2, the T_{eff} and $\log g$ derived from Geneva 7-color photometry in column 3, the final adopted T_{eff} and $\log g$ in col. 4, the derived microturbulent velocity, radial velocity and rotational velocity and a spectral type estimated from T_{eff} in columns 5, 6, 7 and 8

Table 6. Atomic data and their references

Elem.	λ (Å)	$E_{\text{low}}(\text{cm}^{-1})$	$\log gf$	Ref.
Helium				
He I	4713.139	169086.859	−1.277	1(N)
He I	4713.156	169086.938	−1.498	1(N)
He I	4713.376	169087.922	−1.975	1(N)
He I	4921.931	171135.000	−0.443	1(N)
He I	5015.678	166277.547	−0.820	1(N)
Carbon				
C I	4771.742	60393.140	−1.866	2(N)
C I	4932.049	61981.820	−1.658	2(N)
C I	5039.055	64086.920	−1.791	2(N)
C I	5052.167	61981.820	−1.304	2(N)
Oxygen				
O I	4655.356	86632.016	−1.900	2(N)
O I	4773.755	86632.016	−1.667	2(N)
O I	4967.884	86632.016	−1.865	2(N)
O I	4967.884	86632.016	−1.660	2(N)
O I	4968.793	86632.016	−1.961	2(N)
O I	4968.793	86632.016	−1.375	2(N)
O I	5019.290	86632.016	−1.871	2(N)
O I	5020.218	86632.016	−1.725	2(N)

Table 6—Continued

Elem.	λ (Å)	$E_{\text{low}}(\text{cm}^{-1})$	$\log gf$	Ref.
O I	5329.096	86623.945	−1.938	2(N)
O I	5329.098	86623.945	−1.586	2(N)
O I	5329.107	86623.945	−1.695	2(N)
O I	5329.677	86632.016	−1.473	2(N)
O I	5329.688	86632.016	−1.269	2(N)
O I	5330.735	86632.016	−1.570	2(N)
O I	5330.737	86632.016	−0.984	2(N)
Magnesium				
Mg I	4702.991	35051.266	−0.440	3(N)
Mg I	5167.321	21850.404	−0.870	3(N)
Mg I	5172.684	21870.465	−0.393	3(N)
Mg I	5183.604	21911.178	−0.167	3(N)
Mg II	4534.279	93802.281	−1.050	4(V)
Mg II	4534.304	93802.281	−0.940	4(V)
Mg II	4739.593	93310.289	−0.662	3(N)
Mg II	4739.709	93310.289	−0.816	3(N)
Mg II	4851.070	93802.281	−0.790	4(V)
Mg II	4851.099	93802.281	−0.680	4(V)
Mg II	5264.220	93310.289	−0.374	3(N)
Mg II	5264.364	93310.289	−0.529	3(N)

Table 6—Continued

Elem.	λ (Å)	$E_{\text{low}}(\text{cm}^{-1})$	$\log gf$	Ref.
Silicon				
Si II	4621.418	101020.938	−0.608	5(N)
Si II	4621.722	101029.008	−0.453	5(N)
Si II	5041.024	81191.344	0.029	5(N)
Si II	5055.984	81251.320	0.523	5(N)
Si II	5056.317	81251.320	−0.492	5(N)
Si II	5185.520	103553.523	−0.302	5(N)
Phosphorus				
P II	4554.854	106005.445	0.005	6(V)
P II	4558.095	106005.445	−0.056	6(V)
P II	4588.032	103343.820	0.575	6(V)
P II	4589.846	103166.383	0.500	6(V)
P II	4595.515	106005.445	−0.187	6(V)
P II	4602.069	103666.438	0.799	6(V)
P II	4679.028	106005.445	−0.404	6(V)
P II	5040.805	107925.047	−0.120	7(V)
P II	5191.393	86744.930	−0.824	8(V)
P II	5253.479	88890.367	0.291	8(V)
P II	5296.077	87124.008	−0.134	8(V)
P II	5316.055	86744.930	−0.341	8(V)

Table 6—Continued

Elem.	λ (Å)	$E_{\text{low}}(\text{cm}^{-1})$	$\log gf$	Ref.
P II	5344.729	86599.758	−0.329	8(V)
Sulphur				
S II	4524.675	121528.72	−0.746	9(N)
S II	4524.941	121530.02	0.033	9(N)
S II	4552.410	121528.72	−0.208	9(N)
S II	4656.757	109560.69	−0.827	9(N)
S II	4716.271	109831.59	−0.365	9(N)
S II	4792.007	130134.16	−0.120	9(N)
S II	4815.552	110272.125	0.068	9(N)
S II	4917.198	112937.570	−0.375	9(N)
S II	4991.969	109831.590	−0.398	9(N)
S II	5009.567	109831.590	−0.234	9(N)
S II	5014.042	113461.540	0.046	9(N)
S II	5032.434	110268.600	0.188	9(N)
S II	5201.027	121528.720	0.089	9(N)
S II	5201.379	121530.020	−0.713	9(N)
S II	5212.267	121528.720	−1.446	9(N)
S II	5212.620	121530.020	0.316	9(N)
S II	5320.723	121530.020	0.431	9(N)
Argon				

Table 6—Continued

Elem.	λ (Å)	$E_{\text{low}}(\text{cm}^{-1})$	$\log gf$	Ref.
Ar II	4579.349	139258.339	−0.300	7(N)
Ar II	4806.021	134241.739	0.210	7(N)
Ar II	5009.334	135085.996	−0.467	7(N)
Calcium				
Ca II	5001.479	60531.910	−0.507	10(V)
Ca II	5019.971	60612.566	−0.247	10(V)
Ca II	5307.224	60612.566	−0.848	10(V)
Ca II	5339.188	68057.062	−0.447	10(V)
Scandium				
Sc II ^{hfs}	4670.400	10944.560	−1.178	11(VK)
Sc II ^{hfs}	4670.403	10944.560	−1.349	11(VK)
Sc II ^{hfs}	4670.405	10944.560	−1.556	11(VK)
Sc II ^{hfs}	4670.408	10944.560	−1.827	11(VK)
Sc II ^{hfs}	4670.409	10944.560	−1.918	11(VK)
Sc II ^{hfs}	4670.410	10944.560	−2.245	11(VK)
Sc II ^{hfs}	4670.410	10944.560	−1.735	11(VK)
Sc II ^{hfs}	4670.412	10944.560	−1.702	11(VK)
Sc II ^{hfs}	4670.413	10944.560	−1.761	VK
Sc II ^{hfs}	4670.414	10944.560	−1.944	VK
Sc II ^{hfs}	4670.416	10944.560	−2.023	VK

Table 6—Continued

Elem.	λ (Å)	$E_{\text{low}}(\text{cm}^{-1})$	$\log gf$	Ref.
Sc II ^{hfs}	4670.416	10944.560	−2.120	VK
Sc II ^{hfs}	4670.416	10944.560	−2.918	VK
Sc II ^{hfs}	4670.417	10944.560	−2.266	11(VK)
Sc II ^{hfs}	4670.417	10944.560	−2.500	11(VK)
Sc II ^{hfs}	5031.010	10944.560	−1.400	11(VK)
Sc II ^{hfs}	5031.013	10944.560	−1.416	11(VK)
Sc II ^{hfs}	5031.013	10944.560	−1.671	11(VK)
Sc II ^{hfs}	5031.017	10944.560	−1.671	11(VK)
Sc II ^{hfs}	5031.017	10944.560	−1.296	11(VK)
Sc II ^{hfs}	5031.017	10944.560	−2.111	11(VK)
Sc II ^{hfs}	5031.023	10944.560	−1.216	11(VK)
Sc II ^{hfs}	5031.023	10944.560	−1.412	11(VK)
Sc II ^{hfs}	5031.030	10944.560	−0.923	11(VK)
Sc II	5239.813	11736.360	−0.765	11(V)
Sc II ^{hfs}	5640.989	12101.500	−1.654	11(VK)
Sc II ^{hfs}	5640.996	12101.500	−2.143	11(VK)
Sc II ^{hfs}	5641.001	12101.500	−1.947	11(VK)
Sc II ^{hfs}	5641.001	12101.500	−2.842	11(VK)
Sc II ^{hfs}	5641.006	12101.500	−2.027	11(VK)
Sc II ^{hfs}	5641.010	12101.500	−2.402	11(VK)

Table 6—Continued

Elem.	λ (Å)	$E_{\text{low}}(\text{cm}^{-1})$	$\log gf$	Ref.
Sc II ^{hfs}	5641.010	12101.500	−2.402	11(VK)
Sc II ^{hfs}	5641.014	12101.500	−2.147	11(VK)
Sc II ^{hfs}	5641.016	12101.500	−2.131	11(VK)
Sc II ^{hfs}	5657.886	12154.420	−1.229	11(VK)
Sc II ^{hfs}	5657.888	12154.420	−1.799	11(VK)
Sc II ^{hfs}	5657.893	12154.420	−1.799	11(VK)
Sc II ^{hfs}	5657.894	12154.420	−1.627	11(VK)
Sc II ^{hfs}	5657.895	12154.420	−1.641	11(VK)
Sc II ^{hfs}	5657.899	12154.420	−1.641	11(VK)
Sc II ^{hfs}	5657.901	12154.420	−2.323	11(VK)
Sc II ^{hfs}	5657.902	12154.420	−1.652	11(VK)
Sc II ^{hfs}	5657.904	12154.420	−1.652	11(VK)
Sc II ^{hfs}	5657.906	12154.420	−1.825	11(VK)
Sc II ^{hfs}	5657.906	12154.420	−3.749	11(VK)
Sc II ^{hfs}	5657.908	12154.420	−1.825	11(VK)
Sc II ^{hfs}	5657.909	12154.420	−2.001	11(VK)
Sc II ^{hfs}	5658.351	12074.100	−1.588	11(VK)
Sc II ^{hfs}	5658.363	12074.100	−1.685	11(VK)
Sc II ^{hfs}	5658.373	12074.100	−1.810	11(VK)
Sc II ^{hfs}	5667.136	12101.500	−1.903	11(VK)

Table 6—Continued

Elem.	λ (Å)	$E_{\text{low}}(\text{cm}^{-1})$	$\log gf$	Ref.
<hr/>				
Sc II ^{hfs}	5667.141	12101.500	−2.099	11(VK)
Sc II ^{hfs}	5667.148	12101.500	−2.099	11(VK)
Sc II ^{hfs}	5667.154	12101.500	−3.284	11(VK)
Sc II ^{hfs}	5667.157	12101.500	−2.103	11(VK)
Sc II ^{hfs}	5667.163	12101.500	−2.103	11(VK)
Sc II ^{hfs}	5667.167	12101.500	−2.358	11(VK)
Sc II ^{hfs}	5669.038	12101.500	−1.580	11(VK)
Sc II ^{hfs}	5669.044	12101.500	−1.677	11(VK)
Sc II ^{hfs}	5669.047	12101.500	−1.802	11(VK)
Sc II ^{hfs}	5684.190	12154.420	−1.597	11(VK)
Sc II ^{hfs}	5684.191	12154.420	−2.086	11(VK)
Sc II ^{hfs}	5684.193	12154.420	−2.785	11(VK)
Sc II ^{hfs}	5684.204	12154.420	−1.890	11(VK)
Sc II ^{hfs}	5684.205	12154.420	−1.970	11(VK)
Sc II ^{hfs}	5684.206	12154.420	−2.345	11(VK)
Sc II ^{hfs}	5684.215	12154.420	−2.345	11(VK)
Sc II ^{hfs}	5684.216	12154.420	−2.090	11(VK)
Sc II ^{hfs}	5684.217	12154.420	−2.074	11(VK)
Titanium				
Ti II	4529.474	12679.036	−1.640	V

Table 6—Continued

Elem.	λ (Å)	$E_{\text{low}}(\text{cm}^{-1})$	$\log gf$	Ref.
<hr/>				
Ti II	4533.960	9977.078	−0.530	12(V)
Ti II	4549.617	12775.822	−0.110	V
Ti II	4563.757	9848.029	−0.690	V
Ti II	4571.968	12679.036	−0.320	V
Ti II	4779.985	16518.236	−1.260	V
Ti II	4805.085	16623.088	−0.960	V
Ti II	4855.905	24962.859	−1.470	12(V)
Ti II	4865.611	9001.148	−2.790	12(V)
Ti II	4874.009	24962.859	−0.800	12(V)
Ti II	4911.193	25196.762	−0.610	V
Ti II	5154.068	12630.643	−1.750	12(V)
Ti II	5185.902	15268.075	−1.490	12(V)
Ti II	5188.680	12759.691	−1.050	V
Ti II	5211.530	20891.660	−1.165	12(V)
Ti II	5226.539	12630.643	−1.260	12(V)
Ti II	5336.771	12759.691	−1.590	V
Chromium				
Cr II	4554.988	32834.832	−1.491	V
Cr II	4558.650	32850.961	−0.662	V
Cr II	4565.739	32600.930	−1.982	V

Table 6—Continued

Elem.	λ (Å)	$E_{\text{low}}(\text{cm}^{-1})$	$\log gf$	Ref.
Cr II	4588.199	32834.832	−0.845	V
Cr II	4592.049	32859.027	−1.473	V
Cr II	4616.629	32842.898	−1.576	V
Cr II	4618.803	32859.027	−1.084	V
Cr II	4634.070	32842.898	−1.236	V
Cr II	4812.337	31165.264	−2.125	V
Cr II	4824.127	31221.723	−1.085	V
Cr II	4836.229	31116.871	−2.042	V
Cr II	4848.235	31168.580	−1.280	V
Cr II	4856.186	31084.609	−2.171	V
Cr II	4860.202	31221.723	−2.193	V
Cr II	4864.326	31116.871	−1.470	V
Cr II	4876.399	31084.609	−1.580	V
Cr II	4876.473	31165.264	−2.093	V
Cr II	5237.329	86782.039	−0.740	V
Cr II	5274.964	32834.832	−1.559	V
Cr II	5305.853	30866.838	−2.160	V
Cr II	5308.408	32834.832	−2.058	V
Cr II	5313.563	32854.950	−1.650	13(N)
Cr II	5334.869	32842.898	−1.826	V

Table 6—Continued

Elem.	λ (Å)	$E_{\text{low}}(\text{cm}^{-1})$	$\log gf$	Ref.
Manganese				
Mn I ^{hfs}	4754.022	18402.461	−0.653	VK
Mn I ^{hfs}	4754.033	18402.461	−0.793	VK
Mn I ^{hfs}	4754.043	18402.461	−0.951	VK
Mn I ^{hfs}	4754.051	18402.461	−1.135	VK
Mn I ^{hfs}	4754.054	18402.461	−1.571	VK
Mn I ^{hfs}	4754.059	18402.461	−1.357	VK
Mn I ^{hfs}	4754.060	18402.461	−1.395	VK
Mn I ^{hfs}	4754.064	18402.461	−1.369	VK
Mn I ^{hfs}	4754.066	18402.461	−1.642	VK
Mn I ^{hfs}	4754.068	18402.461	−1.436	VK
Mn I ^{hfs}	4754.070	18402.461	−1.612	VK
Mn I ^{hfs}	4754.079	18402.461	−2.390	VK
Mn I ^{hfs}	4754.081	18402.461	−2.311	VK
Mn I ^{hfs}	4754.081	18402.461	−2.788	VK
Mn I ^{hfs}	4754.082	18402.461	−2.436	VK
Mn I ^{hfs}	4761.499	23818.869	−1.025	VK
Mn I ^{hfs}	4761.507	23818.869	−0.564	VK
Mn I ^{hfs}	4761.511	23818.869	−0.928	VK
Mn I ^{hfs}	4761.519	23818.869	−1.041	VK

Table 6—Continued

Elem.	λ (Å)	$E_{\text{low}}(\text{cm}^{-1})$	$\log gf$	Ref.
Mn I ^{hfs}	4761.524	23818.869	−0.928	VK
Mn I ^{hfs}	4761.536	23818.869	−1.472	VK
Mn I ^{hfs}	4762.347	23296.670	−0.177	VK
Mn I ^{hfs}	4762.355	23296.670	−1.273	VK
Mn I ^{hfs}	4762.360	23296.670	−0.281	VK
Mn I ^{hfs}	4762.361	23296.670	−2.688	VK
Mn I ^{hfs}	4762.367	23296.670	−1.085	VK
Mn I ^{hfs}	4762.371	23296.670	−0.394	VK
Mn I ^{hfs}	4762.373	23296.670	−2.353	VK
Mn I ^{hfs}	4762.377	23296.670	−1.047	VK
Mn I ^{hfs}	4762.381	23296.670	−0.516	VK
Mn I ^{hfs}	4762.382	23296.670	−2.256	VK
Mn I ^{hfs}	4762.385	23296.670	−1.102	VK
Mn I ^{hfs}	4762.388	23296.670	−0.646	VK
Mn I ^{hfs}	4762.389	23296.670	−2.387	VK
Mn I ^{hfs}	4762.391	23296.670	−1.290	VK
Mn I ^{hfs}	4762.393	23296.670	−0.779	VK
Mn I ^{hfs}	4765.831	23719.520	−0.595	VK
Mn I ^{hfs}	4765.842	23719.520	−1.284	VK
Mn I ^{hfs}	4765.843	23719.520	−0.807	VK

Table 6—Continued

Elem.	λ (Å)	$E_{\text{low}}(\text{cm}^{-1})$	$\log gf$	Ref.
Mn I ^{hfs}	4765.851	23719.520	−2.238	VK
Mn I ^{hfs}	4765.852	23719.520	−1.080	VK
Mn I ^{hfs}	4765.852	23719.520	−1.138	VK
Mn I ^{hfs}	4765.859	23719.520	−1.490	VK
Mn I ^{hfs}	4765.859	23719.520	−1.159	VK
Mn I ^{hfs}	4765.859	23719.520	−1.858	VK
Mn I ^{hfs}	4765.863	23719.520	−1.682	VK
Mn I ^{hfs}	4765.864	23719.520	−1.314	VK
Mn I ^{hfs}	4765.866	23719.520	−1.636	VK
Mn I ^{hfs}	4766.402	23549.199	−0.467	VK
Mn I ^{hfs}	4766.410	23549.199	−1.385	VK
Mn I ^{hfs}	4766.414	23549.199	−0.607	VK
Mn I ^{hfs}	4766.417	23549.199	−2.602	VK
Mn I ^{hfs}	4766.420	23549.199	−1.209	VK
Mn I ^{hfs}	4766.423	23549.199	−0.765	VK
Mn I ^{hfs}	4766.426	23549.199	−2.250	VK
Mn I ^{hfs}	4766.429	23549.199	−1.183	VK
Mn I ^{hfs}	4766.431	23549.199	−0.949	VK
Mn I ^{hfs}	4766.433	23549.199	−2.125	VK
Mn I ^{hfs}	4766.435	23549.199	−1.250	VK

Table 6—Continued

Elem.	λ (Å)	$E_{\text{low}}(\text{cm}^{-1})$	$\log gf$	Ref.
Mn I ^{hfs}	4766.436	23549.199	−1.171	VK
Mn I ^{hfs}	4766.437	23549.199	−2.204	VK
Mn I ^{hfs}	4766.439	23549.199	−1.456	VK
Mn I ^{hfs}	4766.439	23549.199	−1.426	VK
Mn I ^{hfs}	4783.391	18531.641	−1.559	VK
Mn I ^{hfs}	4783.403	18531.641	−1.377	VK
Mn I ^{hfs}	4783.414	18531.641	−1.346	VK
Mn I ^{hfs}	4783.415	18531.641	−0.567	VK
Mn I ^{hfs}	4783.423	18531.641	−1.411	VK
Mn I ^{hfs}	4783.424	18531.641	−0.738	VK
Mn I ^{hfs}	4783.430	18531.641	−0.923	VK
Mn I ^{hfs}	4783.431	18531.641	−1.609	VK
Mn I ^{hfs}	4783.436	18531.641	−1.115	VK
Mn I ^{hfs}	4783.439	18531.641	−1.290	VK
Mn I ^{hfs}	4783.442	18531.641	−1.354	VK
Mn I ^{hfs}	4783.448	18531.641	−1.559	VK
Mn I ^{hfs}	4783.450	18531.641	−1.609	VK
Mn I ^{hfs}	4783.451	18531.641	−1.377	VK
Mn I ^{hfs}	4783.452	18531.641	−1.411	VK
Mn I ^{hfs}	4783.452	18531.641	−1.346	VK

Table 6—Continued

Elem.	λ (Å)	$E_{\text{low}}(\text{cm}^{-1})$	$\log gf$	Ref.
Mn I ^{hfs}	4823.469	18705.369	−2.969	VK
Mn I ^{hfs}	4823.484	18705.369	−2.634	VK
Mn I ^{hfs}	4823.490	18705.369	−1.554	VK
Mn I ^{hfs}	4823.498	18705.369	−2.537	VK
Mn I ^{hfs}	4823.502	18705.369	−1.366	VK
Mn I ^{hfs}	4823.510	18705.369	−2.668	VK
Mn I ^{hfs}	4823.512	18705.369	−1.328	VK
Mn I ^{hfs}	4823.515	18705.369	−0.458	VK
Mn I ^{hfs}	4823.521	18705.369	−1.383	VK
Mn I ^{hfs}	4823.523	18705.369	−0.562	VK
Mn I ^{hfs}	4823.527	18705.369	−1.571	VK
Mn I ^{hfs}	4823.530	18705.369	−0.675	VK
Mn I ^{hfs}	4823.535	18705.369	−0.797	VK
Mn I ^{hfs}	4823.537	18705.369	−0.927	VK
Mn I ^{hfs}	4823.538	18705.369	−1.060	VK
Mn II	4755.727	43529.742	−1.242	V
Mn II	4762.789	43529.742	−2.528	V
Mn II	4764.728	43537.809	−1.351	V
Mn II	4806.623	43699.121	−1.848	V
Mn II	5295.384	79542.406	0.360	V

Table 6—Continued

Elem.	λ (Å)	$E_{\text{low}}(\text{cm}^{-1})$	$\log gf$	Ref.
<hr/>				
Mn II	5295.412	79542.406	0.360	V
Mn II	5297.000	79550.461	−0.214	V
Mn II	5297.028	79550.461	0.427	V
Mn II	5297.058	79550.461	0.623	V
Mn II	5299.302	79558.531	−0.418	V
Mn II	5299.330	79558.531	0.401	V
Mn II	5299.386	79558.531	0.827	V
Mn II	5302.346	79566.594	−0.817	V
Mn II	5302.402	79566.594	0.225	V
Mn II	5302.431	79566.594	0.997	V
Iron				
Fe I	4525.137	29060.156	−0.234	K
Fe I	4528.613	17550.625	−0.822	14(N)
Fe I	4859.741	23188.439	−0.764	14(N)
Fe I	4871.317	23110.939	−0.362	14(N)
Fe I	4872.136	23244.898	−0.567	14(N)
Fe I	4890.754	23188.439	−0.394	14(N)
Fe I	4891.492	22994.867	−0.112	14(N)
Fe I	4918.993	23107.785	−0.342	14(N)
Fe I	4920.502	22841.621	0.068	14(N)

Table 6—Continued

Elem.	λ (Å)	$E_{\text{low}}(\text{cm}^{-1})$	$\log gf$	Ref.
Fe I	4957.298	22994.867	−0.408	14(N)
Fe I	4957.596	22648.049	0.233	14(N)
Fe I	4982.499	33092.930	0.156	K
Fe I	5001.862	31302.379	−0.010	14(N)
Fe I	5005.712	31326.574	0.029	K
Fe I	5006.117	22845.869	−0.615	14(N)
Fe I	5167.487	11977.334	−1.118	14(N)
Fe I	5191.454	24503.125	−0.551	14(N)
Fe I	5192.343	24180.502	−0.421	14(N)
Fe I	5226.862	24503.125	−0.555	14(N)
Fe I	5227.189	12558.053	−1.228	14(N)
Fe I	5232.939	23711.456	−0.057	14(N)
Fe I	5266.555	24180.862	−0.385	14(N)
Fe I	5269.537	6928.303	−1.321	14(N)
Fe I	5270.356	12969.396	−1.339	14(N)
Fe I	5283.621	26140.179	−0.525	14(N)
Fe I	5324.178	25898.463	−0.103	14(N)
Fe I	5328.038	7379.973	−1.466	14(N)
Fe I	5615.644	26874.395	0.050	14(N)
Fe II	4508.288	23031.301	−2.210	K

Table 6—Continued

Elem.	λ (Å)	$E_{\text{low}}(\text{cm}^{-1})$	$\log gf$	Ref.
Fe II	4515.339	22938.410	−2.540	15(V)
Fe II	4520.224	22639.982	−2.617	15(V)
Fe II	4522.634	22938.410	−2.169	15(V)
Fe II	4534.168	23035.195	−3.364	15(V)
Fe II	4541.524	23035.195	−2.973	15(V)
Fe II	4549.192	47675.430	−1.767	15(V)
Fe II	4549.474	22809.359	−2.016	15(V)
Fe II	4555.893	22809.359	−2.421	15(V)
Fe II	4576.340	22938.410	−2.976	15(V)
Fe II	4579.527	50216.078	−2.343	15(V)
Fe II	4580.063	20833.301	−3.904	15(V)
Fe II	4582.835	22938.410	−3.224	15(V)
Fe II	4583.837	22639.982	−1.867	15(V)
Fe II	4596.015	50216.078	−1.956	15(V)
Fe II	4598.494	62943.508	−1.536	15(V)
Fe II	4620.521	22809.359	−3.315	15(V)
Fe II	4625.893	48038.383	−2.549	15(V)
Fe II	4629.339	22639.982	−2.478	15(V)
Fe II	4635.316	48038.383	−1.578	15(V)
Fe II	4638.050	62169.219	−1.536	15(V)

Table 6—Continued

Elem.	λ (Å)	$E_{\text{low}}(\text{cm}^{-1})$	$\log gf$	Ref.
Fe II	4640.812	62169.219	−1.737	15(V)
Fe II	4656.981	23317.488	−3.643	15(V)
Fe II	4663.708	23317.488	−3.889	15(V)
Fe II	4666.758	22809.359	−3.368	15(V)
Fe II	4670.182	20833.301	−4.073	15(V)
Fe II	4731.453	23317.488	−3.127	15(V)
Fe II	4826.683	82978.320	−0.500	15(V)
Fe II	4855.548	21809.232	−4.443	15(V)
Fe II	4871.277	21809.232	−4.236	15(V)
Fe II	4908.151	83309.016	−0.272	15(V)
Fe II	4913.292	82978.320	0.050	15(V)
Fe II	4923.927	23317.633	−1.320	K
Fe II	4948.096	83139.625	−0.218	15(V)
Fe II	4951.584	83139.625	0.211	15(V)
Fe II	4977.035	83559.039	−0.039	15(V)
Fe II	4984.488	83309.016	0.078	15(V)
Fe II	4990.509	83309.016	0.195	15(V)
Fe II	4993.358	22639.982	−3.684	15(V)
Fe II	4999.180	82857.336	−0.435	15(V)
Fe II	5001.959	82857.336	0.916	15(V)

Table 6—Continued

Elem.	λ (Å)	$E_{\text{low}}(\text{cm}^{-1})$	$\log gf$	Ref.
Fe II	5004.195	82857.336	0.504	15(V)
Fe II	5006.841	83712.281	−0.362	15(V)
Fe II	5007.447	83728.414	−0.460	15(V)
Fe II	5015.755	83462.250	−0.028	15(V)
Fe II	5018.440	23317.488	−1.345	15(V)
Fe II	5021.594	82978.320	−0.191	15(V)
Fe II	5022.420	83462.250	−0.073	15(V)
Fe II	5022.792	82978.320	−0.092	15(V)
Fe II	5030.630	82978.320	0.431	15(V)
Fe II	5032.712	83817.141	0.077	15(V)
Fe II	5035.708	82978.320	0.632	15(V)
Fe II	5045.114	83139.625	−0.002	15(V)
Fe II	5047.641	83139.625	−0.235	15(V)
Fe II	5061.718	83139.625	0.284	15(V)
Fe II	5067.893	83309.016	−0.078	15(V)
Fe II	5070.899	83139.625	0.268	15(V)
Fe II	5143.880	84268.805	−0.205	15(V)
Fe II	5144.355	84422.055	0.307	15(V)
Fe II	5145.772	83994.578	−0.213	15(V)
Fe II	5145.817	83994.578	−0.144	15(V)

Table 6—Continued

Elem.	λ (Å)	$E_{\text{low}}(\text{cm}^{-1})$	$\log gf$	Ref.
Fe II	5148.907	83994.578	−0.417	15(V)
Fe II	5149.465	84268.805	0.554	15(V)
Fe II	5150.489	84268.805	−0.078	15(V)
Fe II	5157.282	84325.266	−0.173	15(V)
Fe II	5160.839	44917.016	−2.559	15(V)
Fe II	5166.555	84325.266	−0.045	15(V)
Fe II	5169.033	23317.635	−0.870	14(N)
Fe II	5170.777	84325.266	−0.330	15(V)
Fe II	5177.020	83712.281	−0.197	15(V)
Fe II	5178.371	84131.695	−0.334	15(V)
Fe II	5180.314	83817.141	−0.088	15(V)
Fe II	5186.873	84422.055	−0.194	15(V)
Fe II	5194.892	84422.055	−0.108	15(V)
Fe II	5197.577	26051.709	−2.348	15(V)
Fe II	5199.122	83712.281	0.121	15(V)
Fe II	5200.804	83817.141	−0.036	15(V)
Fe II	5203.638	83817.141	−0.115	15(V)
Fe II	5212.841	84849.531	−0.300	15(V)
Fe II	5213.960	84526.898	−0.258	15(V)
Fe II	5215.349	83712.281	0.000	15(V)

Table 6—Continued

Elem.	λ (Å)	$E_{\text{low}}(\text{cm}^{-1})$	$\log gf$	Ref.
Fe II	5215.844	83728.414	−0.159	15(V)
Fe II	5216.854	84712.414	0.478	15(V)
Fe II	5216.863	84526.898	0.670	15(V)
Fe II	5218.842	83728.414	−0.165	15(V)
Fe II	5222.361	84849.531	−0.281	15(V)
Fe II	5223.260	83817.141	−0.169	15(V)
Fe II	5227.323	84849.531	0.188	15(V)
Fe II	5227.481	84301.070	0.846	15(V)
Fe II	5228.896	84268.805	−0.300	15(V)
Fe II	5232.787	83728.414	−0.082	15(V)
Fe II	5234.625	25979.119	−2.279	15(V)
Fe II	5237.950	84268.805	0.104	15(V)
Fe II	5247.952	84938.250	0.550	15(V)
Fe II	5257.122	84688.219	0.156	15(V)
Fe II	5260.259	84034.906	1.088	K
Fe II	5264.177	84712.414	0.297	15(V)
Fe II	5264.812	26051.709	−3.133	15(V)
Fe II	5270.027	84712.414	−0.197	15(V)
Fe II	5272.397	48038.383	−2.009	15(V)
Fe II	5276.002	25801.676	−2.213	15(V)

Table 6—Continued

Elem.	λ (Å)	$E_{\text{low}}(\text{cm}^{-1})$	$\log gf$	Ref.
Fe II	5284.109	23317.488	−3.195	15(V)
Fe II	5291.666	84526.898	0.544	15(V)
Fe II	5306.180	84873.719	0.044	15(V)
Fe II	5316.225	84034.906	0.340	15(V)
Fe II	5316.615	25430.662	−2.014	15(V)
Fe II	5316.784	25979.119	−2.783	15(V)
Fe II	5318.057	84526.898	−0.226	15(V)
Fe II	5325.553	25979.119	−3.324	15(V)
Fe II	5337.732	26051.709	−3.788	15(V)
Fe II	5339.585	84301.070	0.517	15(V)
Fe II	5643.880	61725.609	−1.346	15(V)
Fe II	5645.392	85188.281	0.193	15(V)
Fe II	5648.904	85188.281	−0.165	15(V)
Fe II	5690.994	86123.891	−0.175	15(V)
Fe II	5726.557	86414.242	−0.035	15(V)
Fe II	5780.128	86123.891	0.421	15(V)
Fe II	5783.630	86414.242	0.365	15(V)
Fe II	5784.448	86599.758	0.145	15(V)
Nickel				
Ni I	4592.522	28576.225	−0.370	16(V)

Table 6—Continued

Elem.	λ (Å)	$E_{\text{low}}(\text{cm}^{-1})$	$\log gf$	Ref.
Ni I	4604.982	28068.096	−0.250	16(V)
Ni I	4648.646	27584.162	−0.100	16(V)
Ni I	4686.207	29011.762	−0.580	16(V)
Ni I	4701.530	32971.945	−0.390	V
Ni I	4714.408	27261.541	0.260	16(V)
Ni I	4715.757	28576.225	−0.320	16(V)
Ni I	4786.531	27584.162	−0.160	16(V)
Ni I	4829.016	28568.158	−0.330	V
Ni I	4831.169	29084.354	−0.320	16(V)
Ni I	4980.166	29084.354	0.070	16(V)
Ni I	4984.112	30616.807	0.226	V
Ni I	5017.568	28543.963	−0.020	16(V)
Ni I	5035.357	29318.254	0.290	16(V)
Ni I	5035.967	29479.564	−0.234	V
Ni I	5142.775	29890.908	−0.231	V
Ni I	5142.926	29834.447	−0.732	V
Ni I	5146.480	29890.908	−0.060	V
Ni I	5155.125	31439.492	−0.650	V
Ni I	5155.762	31439.492	0.011	V
Ni I	5168.656	29834.447	−0.430	16(V)

Table 6—Continued

Elem.	λ (Å)	$E_{\text{low}}(\text{cm}^{-1})$	$\log gf$	Ref.
<hr/>				
Ni I	5176.559	31439.492	−0.440	V
Ni I	5715.066	32971.945	−0.352	V
Ni II	4679.159	56370.090	−1.748	V
Ni II	5017.723	98972.297	0.500	V
Yttrium				
Y II	4883.684	8743.050	0.070	17(N)
Y II	4900.120	8331.707	−0.090	17(N)
Y II	5196.422	14098.572	−0.880	V
Y II	5200.406	8001.020	−0.570	V
Y II	5205.724	8331.707	−0.340	17(N)
Zirconium				
Zr II	5191.592	14163.097	−0.712	18(V)
Zr II	5311.784	14163.097	−1.500	V
Zr II	5350.089	14735.750	−1.240	18(V)
Zr II	5350.350	14300.210	−1.160	19(V)
Xenon				
Xe II	4844.330	93068.312	0.220	20(V)
Xe II	4876.500	109562.352	0.254	21(V)
Xe II	4921.480	102803.430	0.200	21(V)
Xe II	5292.220	93068.312	0.100	21(V)

Table 6—Continued

Elem.	λ (Å)	$E_{\text{low}}(\text{cm}^{-1})$	$\log gf$	Ref.
Barium				
Ba II	4524.925	20261.561	−0.391	22(N)
Ba II	4554.029	0.000	0.140	22(N)
Ba II	4899.929	21952.404	−0.130	22(N)
Ba II	4934.076	0.000	−0.160	22(N)
Mercury				
Hg I	5769.593	54071.410	0.630	V

References. — K: via Kurucz’s gfhyperall.dat, V: via VALD2, N: via NIST Atomic Spectra Database, VK: atomic data from VALD2 and $\log gf$ fractions for hfs from Kurucz’s gfhyperall.dat, 1: Wiese & Fuhr (2009), 2: Wiese et al. (1996), 3: Kelleher & Podobedova (2008b), 4: Kurucz & Peytremann (1975), 5: Kelleher & Podobedova (2008a), 6: Miller et al. (1971), 7: Wiese et al. (1969), 8: Hibbert (1988), 9: Podobedova et al. (2009), 10: Theodosiou

(1989), 11: Lawler & Dakin (1989), 12: Pickering et al. (2002), 13: Martin et al. (1988), 14: Fuhr & Wiese (2006) and/or O'Brian et al. (1991), 15: Raassen & Uylings (1998), 16: Wickliffe & Lawler (1997), 17: Fuhr & Wiese (2005), 18: Cowley & Corliss (1983), 19: Ljung et al. (2006), 20: Ryabchikova & Smirnov (1989), 21: Wiese & Martin (1980), 22: Curry (2004)

Table 7. $\text{Log}(X/H)$ absolute abundances for the M6 dwarfs

Star	Star no.	He	C	O	Mg	Si	P	S	Ar	Ca	Sc
HD 160093	33
HD 160167	115	-1.19	-4.68
HD 160188	...	-1.38	-4.75
HD 160222	97	-1.03	-4.41
HD 160259	28	-1.31	-4.47
HD 160260	70	-0.94	-4.27
HD 160297	41	-4.37
HD 160298	94	-1.20	-4.34
HD 160392	17	-1.05	...	-3.11	-4.31	-4.33
HD 318091	5	...	-3.82	...	-4.43	-4.42	-6.27	-9.41
HD 318092	22	-4.28
HD 318093	25	-3.39	-4.59	-4.51	-5.76	...
HD 318094	42	...	-3.43	-3.38	-4.02	-4.37	-5.70	-8.69
HD 318099	29	-3.30	-4.45	-4.43
HD 318101	20	-1.55	...	-3.37	...	-5.02	-4.88	-5.32	-5.13
HD 318103	-3.48	...	-4.40	-4.31	-5.81	-8.65
HD 318110	96	-1.06	-4.45
HD 318111	-3.31	-4.65	-4.34
HD 318112	-3.31	-4.37	-4.45
HD 318113	95	-4.48
HD 318114	64	-3.19	-4.17	-4.45	-5.64	...
HD 318117	37	-4.34
HD 318118	63	...	-3.53	-3.38	-4.48	-4.35	-5.66	-8.64
HD 318126	99	-4.65
CD-32 13092	73	...	-3.07	-3.09	-3.99	-4.41
CD-32 13093	52	-4.15	-4.43	-5.63	...
CD-32 13097	51	-4.15	-4.43	-5.67	...
CD-32 13106	71	...	-3.57	...	-4.20	-4.32	-5.88	-8.71
CD-32 13109	47	...	-3.76	-3.40	-4.30	-4.42	-5.74	-9.22
CD-32 13126	44	-4.06	-4.19	-5.74	...
CD-32 13148	130	...	-3.59	...	-4.25	-4.23	-5.71	-8.78
CPD-32 4693	118	-4.22	-4.41	-5.62	-8.83
CPD-32 4713	48	...	-3.57	-3.18	-4.05	-4.35	-5.77	-8.86
CPD-32 4724	-3.45	-3.34	-4.02	-4.60	-5.55	-8.74
CPD-32 4739	67	...	-3.37	...	-3.49	-8.83
GSC-7380 0206	18	...	-3.40	...	-4.22	-5.67	-8.84
GSC-7380 0281	26	...	-3.30	...	-4.30	-4.47	-5.66	-8.65
GSC-7380-0339	27	...	-3.52	...	-4.37	-4.34	-5.53	-8.75
GSC-7380-0539	31	...	-3.64	...	-4.28	-4.20	-5.75	-8.74
GSC-7380 0766	14	...	-3.44	...	-4.29	-5.67	-8.82
GSC-7380 0986	66	...	-3.51	...	-4.27	-4.33	-5.51	-8.83
GSC-7380-1170	6	-4.40	-4.35	-8.77
GSC-7380 1211	69	...	-3.44	...	-4.24	-4.43	-5.43	-8.75
GSC-7380 1363	-4.38	-4.36	-5.65	-8.95

Table 7—Continued

Star	Star no.	Ti	Cr	Mn	Fe	Ni	Y	Zr	Xe	Ba	Hg
HD 160093	33
HD 160167	115	-4.74
HD 160188	-4.39
HD 160222	97
HD 160259	28	-4.36
HD 160260	70	-4.50
HD 160297	41	...	-6.17	...	-4.42
HD 160298	94	...	-6.17	...	-4.37
HD 160392	17	-7.20	-6.02	...	-4.39
HD 318091	5	-7.08	-5.97	-6.33	-4.51	-5.58	-9.65	-9.03	...
HD 318092	22	...	-6.18	...	-4.36
HD 318093	25	...	-6.21	...	-4.55
HD 318094	42	-7.04	-6.23	...	-4.43	-5.69	-9.72	-9.97	...
HD 318099	29	-7.10	-6.21	...	-4.45
HD 318101	20	-4.47	-5.98
HD 318103	...	-7.05	-6.25	...	-4.55	-5.84	-9.68	-9.61	...
HD 318110	96	-6.93	-6.05	...	-4.29
HD 318111	-6.21	...	-4.42
HD 318112	...	-7.16	-6.09	...	-4.36
HD 318113	95	-6.52	-5.77	...	-4.19
HD 318114	64	-7.02	-6.15	...	-4.40
HD 318117	37	...	-6.38	...	-4.67
HD 318118	63	-7.08	-6.05	...	-4.43	...	-9.28	-9.06	...
HD 318126	99	-5.70	-5.44	-4.36	-4.84	-5.19	-6.35	-6.10	...	-8.05	-5.69
CD-32 13092	73	-7.12	-5.90	-5.66	-4.24	-5.69	-7.81
CD-32 13093	52	-6.98	-6.33	...	-4.50	-5.74
CD-32 13097	51	-7.04	-4.49	-5.72
CD-32 13106	71	-7.08	-6.30	-6.44	-4.61	...	-9.59
CD-32 13109	47	-6.79	-5.71	-6.19	-4.16	-5.27	-9.05	-8.40	...
CD-32 13126	44	-7.19	-6.01	...	-4.58
CD-32 13148	130	-6.98	-6.23	-6.34	-4.53	-5.84	-9.78	-9.56	...
CPD-32 4693	118	-7.05	-6.27	-6.57	-4.46	-5.75	-9.76	-9.38	...
CPD-32 4713	48	-7.17	-6.35	-6.68	-4.65	-5.78	-9.47
CPD-32 4724	...	-6.95	-6.17	...	-4.48	-5.83	-9.77	...
CPD-32 4739	67	-7.12	-6.26	-6.53	-4.52	-5.78	-9.09	...
GSC-7380 0206	18	-7.01	-6.23	-6.45	-4.38	-5.63	-9.65	-9.44	...
GSC-7380 0281	26	-7.05	-6.27	-6.51	-4.51	-5.81	-9.09	...
GSC-7380-0339	27	-6.88	-6.11	-6.45	-4.40	-5.73	-9.52	-9.33	...
GSC-7380-0539	31	-6.95	-6.27	-6.53	-4.55	-5.79	-9.56	-9.46	...
GSC-7380 0766	14	-6.95	-6.19	-6.61	-4.45	-5.74	-9.58	-9.29	...
GSC-7380 0986	66	-6.95	-6.23	-6.70	-4.43	-5.74	-9.66	-9.30	...
GSC-7380-1170	6	-6.94	-6.16	-6.43	-4.40	-5.73	-9.70	-9.27	...
GSC-7380 1211	69	-6.86	-5.98	-6.23	-4.25	-5.61	-9.26	-9.11	...
GSC-7380 1363	...	-7.02	-6.23	-6.57	-4.47	-5.78	-9.67	-9.39	...

Table 8. Abundances for the M6 Dwarfs with respect to the cosmic abundance standards
(Nieva & Przybilla 2012)

Star	Star no.	[He/H]	[C/H]	[O/H]	[Mg/H]	[Si/H]	[Fe/H]
HD 160093	33
HD 160167	115	-0.18	-0.18	-0.26
HD 160188	...	-0.37	-0.25	0.09
HD 160222	97	-0.02	0.09	...
HD 160259	28	-0.30	0.03	0.12
HD 160260	70	0.07	0.23	-0.02
HD 160297	41	0.13	0.06
HD 160298	94	-0.19	0.16	0.11
HD 160392	17	-0.04	...	0.13	0.13	0.17	0.09
HD 318091	5	...	-0.15	...	0.01	0.08	-0.03
HD 318092	22	0.16	...	0.12
HD 318093	25	-0.15	-0.15	-0.01	-0.07
HD 318094	42	...	0.24	-0.14	0.42	0.13	0.05
HD 318099	29	-0.06	-0.01	0.07	0.03
HD 318101	20	-0.54	...	-0.13	...	-0.52	0.01
HD 318103	0.19	...	0.04	0.19	-0.07
HD 318110	96	-0.05	0.05	0.19
HD 318111	-0.07	-0.21	0.16	0.06
HD 318112	-0.07	0.07	0.05	0.12
HD 318113	95	0.02	0.29
HD 318114	64	0.05	0.27	0.05	0.08
HD 318117	37	0.16	-0.19
HD 318118	63	...	0.14	-0.14	-0.04	0.15	0.05
HD 318126	99	-0.15	-0.36
CD-32 13092	73	...	0.60	0.15	0.45	0.09	0.24
CD-32 13093	52	0.29	0.07	-0.02
CD-32 13097	51	0.29	0.07	-0.01
CD-32 13106	71	...	0.10	...	0.24	0.18	-0.13
CD-32 13109	47	...	-0.09	-0.16	0.14	0.08	0.32
CD-32 13126	44	0.38	0.31	-0.10
CD-32 13148	130	...	0.08	...	0.19	0.27	-0.05
CPD-32 4693	118	0.22	0.09	0.02
CPD-32 4713	48	...	0.10	0.06	0.39	0.15	-0.17
CPD-32 4724	0.22	-0.10	0.42	-0.10	0.00
CPD-32 4739	67	...	0.30	...	0.95	...	-0.04
GSC-7380 0206	18	...	0.27	...	0.22	...	0.10
GSC-7380 0281	26	...	0.37	...	0.14	0.03	-0.03
GSC-7380-0339	27	...	0.15	...	0.07	0.16	0.08
GSC-7380-0539	31	...	0.03	...	0.16	0.30	-0.07
GSC-7380 0766	14	...	0.23	...	0.15	...	0.03
GSC-7380 0986	66	...	0.16	...	0.17	0.17	0.05
GSC-7380-1170	6	0.04	0.15	0.08
GSC-7380 1211	69	...	0.23	...	0.20	0.07	0.23
GSC-7380 1363	0.06	0.14	0.01

Table 9. Uncertainties of the abundances for late B stars

Species	$\sigma_{T_{\text{eff}}}$	$\sigma_{\log g}$	$\sigma_{v_{\text{mic}}}$	$\sigma_{\text{norm.}}$	σ_{tot}	$\sigma_{\text{max.}}$
	$\pm 300 \text{ K}$	$\pm 0.10 \text{ dex}$	$0/1 \text{ km s}^{-1}$	$\pm (1/\text{SNR})$		
He	0.10	0.12	0.00	0.01	0.16	...
O	0.02	0.02	0.04	0.02	0.05	0.25
Mg	0.10	0.02	0.00	0.01	0.11	0.16
Si	0.02	0.01	0.03	0.03	0.05	0.10
P	0.01	0.02	0.03	0.01	0.04	...
S	0.04	0.04	0.01	0.04	0.07	...
Ar	0.05	0.04	0.03	0.19	0.20	...
Ti	0.15	0.08	0.07	0.05	0.19	0.21
Cr	0.15	0.11	0.08	0.06	0.21	0.58
Mn	0.05	0.04	0.04	0.05	0.09	...
Fe	0.00	0.01	0.06	0.07	0.09	0.24
Ni	0.09	0.01	0.00	0.16	0.19	...
Y	0.29	0.19	0.08	0.06	0.36	...
Zr	0.16	0.01	0.02	0.03	0.16	...
Xe	0.08	0.10	0.00	0.08	0.15	...
Ba	0.11	0.03	0.14	0.07	0.20	...
Hg	0.06	0.03	0.09	0.48	0.50	...

Table 10. Uncertainties of the abundances for A stars

Species	$\sigma_{T_{\text{eff}}}$ $\pm 150 \text{ K}$	$\sigma_{\log g}$ $\pm 0.10 \text{ dex}$	$\sigma_{v_{\text{mic}}}$ $\pm 0.20 \text{ km s}^{-1}$	$\sigma_{\text{norm.}}$ $\pm (1/\text{SNR})$	σ_{tot}	$\sigma_{\text{max.}}$
C	0.10	0.03	0.01	0.08	0.13	0.14
O	0.01	0.01	0.00	0.04	0.04	0.07
Mg	0.09	0.03	0.01	0.02	0.10	0.16
Si	0.01	0.01	0.01	0.02	0.03	0.06
Ca	0.06	0.02	0.01	0.06	0.09	0.09
Sc	0.06	0.01	0.02	0.06	0.08	0.10
Ti	0.07	0.01	0.02	0.01	0.07	0.11
Cr	0.08	0.00	0.01	0.01	0.08	0.12
Mn	0.04	0.00	0.01	0.04	0.05	0.19
Fe	0.07	0.01	0.02	0.01	0.08	0.13
Ni	0.12	0.03	0.00	0.03	0.13	0.18
Y	0.12	0.00	0.00	0.02	0.12	0.23
Ba	0.16	0.07	0.08	0.04	0.19	0.19

Table 11. Uncertainties of the abundances for F stars

Species	$\sigma_{T_{\text{eff}}}$	$\sigma_{\log g}$	$\sigma_{v_{\text{mic}}}$	$\sigma_{\text{norm.}}$	σ_{tot}	$\sigma_{\text{max.}}$
	$\pm 150 \text{ K}$	$\pm 0.30 \text{ dex}$	$\pm 0.20 \text{ km s}^{-1}$	$\pm (1/\text{SNR})$		
C	0.03	0.09	0.00	0.04	0.10	0.25
Mg	0.14	0.16	0.01	0.02	0.21	0.23
Si	0.04	0.07	0.01	0.16	0.18	0.19
Ca	0.04	0.02	0.05	0.02	0.07	0.12
Sc	0.04	0.11	0.02	0.08	0.13	0.28
Ti	0.06	0.07	0.02	0.04	0.10	0.13
Cr	0.05	0.05	0.02	0.05	0.09	0.14
Mn	0.09	0.01	0.03	0.04	0.11	0.15
Fe	0.06	0.01	0.03	0.05	0.08	0.13
Ni	0.03	0.01	0.01	0.05	0.06	0.12
Zn	0.07	0.04	0.02	0.09	0.13	0.22
Y	0.07	0.08	0.05	0.02	0.12	0.28
Ba	0.10	0.05	0.09	0.03	0.15	0.22

Table 12. Mean abundances with respect to the Sun (Grevesse & Sauval 1998) and
star-to-star abundance variations

Element	A-type stars		A-type stars (except CP stars)		F-type stars		F-type stars (except CP stars)	
	$\langle[X/H]\rangle$	$\sigma([X/H])$	$\langle[X/H]\rangle$	$\sigma([X/H])$	$\langle[X/H]\rangle$	$\sigma([X/H])$	$\langle[X/H]\rangle$	$\sigma([X/H])$
C	−0.10	0.13	−0.05	0.06	0.02	0.05	0.02	0.06
O	−0.15	0.10	−0.12	0.11
Mg	0.18	0.17	0.22	0.18	0.13	0.07	0.12	0.08
Si	0.09	0.11	0.10	0.13	0.08	0.04	0.09	0.03
Ca	−0.12	0.21	−0.08	0.12	0.07	0.09	0.04	0.07
Sc	0.02	0.28	0.11	0.08	0.02	0.07	0.01	0.06
Ti	−0.03	0.12	−0.07	0.08	0.03	0.07	0.01	0.06
Cr	0.25	0.21	0.12	0.11	0.16	0.09	0.13	0.05
Mn	0.24	0.18	0.15	0.17	0.13	0.14	0.08	0.10
Fe	0.04	0.15	−0.04	0.08	0.10	0.07	0.07	0.03
Ni	0.12	0.23	−0.07	0.03	0.04	0.06	0.02	0.05
Y	0.33	0.26	0.24	0.19	0.19	0.16	0.12	0.08
Ba	0.90	0.51	0.46	0.31	0.57	0.10	0.53	0.06

Table 13. Coefficients for the abundances vs. $[\text{Fe}/\text{H}]$

$Y = a[\text{Fe}/\text{H}] + b$			
Y	a	b	$R^2(^*)$
$[\text{C}/\text{Fe}]$	−1.20	−0.04	0.704
$[\text{O}/\text{Fe}]$	−1.60	−0.10	0.998
$[\text{Mg}/\text{Fe}]$	−1.04	0.11	0.369
$[\text{Si}/\text{Fe}]$	−1.19	0.11	0.927
$[\text{Ca}/\text{H}]$	0.65	−0.07	0.297
$[\text{Sc}/\text{Fe}]$	−1.76	0.04	0.722
$[\text{Ti}/\text{H}]$	0.66	−0.05	0.717
$[\text{Cr}/\text{H}]$	1.01	0.11	0.702
$[\text{Mn}/\text{H}]$	1.02	0.06	0.719
$[\text{Ni}/\text{H}]$	0.66	−0.05	0.835
$[\text{Y}/\text{H}]$	1.72	0.04	0.768
$[\text{Ba}/\text{H}]$	2.50	0.41	0.585

$*R^2$: Coefficient of determination

Table 14. Radial velocity variations

Star	Rohlfs et	MJD	MJD	Difference	Radially variable?
	al. (1959)	54250.3494	54256.1309		
	id. no	v_{rad} (km s ⁻¹)	v_{rad} (km s ⁻¹)	$ \Delta v_{\text{rad}} $ (km s ⁻¹)	
HD 160167	115	-10.39	-11.49	1.10	No
HD 160392	17	-8.09	-9.43	1.35	No
HD 318091	5	-7.29	-3.07	4.22	Yes
HD 318093	25	-5.29	-7.30	2.02	No
HD 318094	42	-4.69	-7.29	2.60	No
HD 318099	29	-6.09	-8.08	1.99	No
HD 318101	20	-8.39	-7.98	0.41	No
HD 318103	...	-8.79	-6.47	2.32	No
HD 318111	96	-5.29	-6.84	1.56	No
HD 318112	...	-10.29	-11.54	1.25	No
HD 318114	64	-8.59	-13.06	4.47	Yes
HD 318118	63	-6.69	-5.25	1.44	No
HD 318126	99	18.31	-20.10	38.41	Yes
CD-32 13093	52	-5.19	-4.62	0.52	No
CD-32 13097	51	1.71	-1.93	3.63	Yes
CD-32 13106	71	-0.29	-1.01	0.72	No
CD-32 13109	47	-3.39	-0.37	3.02	Yes
CD-32 13148	130	-4.89	-7.90	3.01	Yes
CPD-32 4693	118	-6.49	-6.91	0.42	No
CPD-32 4713	48	-3.49	-4.91	1.42	No
CPD-32 4724	...	-8.49	-9.21	0.72	No
CPD-32 4739	67	-8.19	-8.38	0.19	No
GSC07380-00206	18	-11.89	-10.80	1.09	No
GSC07380-00281	26	-7.59	-6.97	0.62	No
GSC07380-00339	27	-9.19	-9.26	0.07	No
GSC07380-00539	31	-7.72	-2.84	4.87	Yes
GSC07380-00766	14	-10.59	-9.55	1.04	No
GSC07380-00986	66	-9.89	-9.97	0.08	No
GSC 07380-01170	6	-9.09	-9.17	0.08	No

Table 14—Continued

Star	Rohlfs et	MJD	MJD	Difference $ \Delta v_{\text{rad}} $ (km s ^{−1})	Radially variable?
	al. (1959) id. no	54250.3494 v_{rad} (km s ^{−1})	54256.1309 v_{rad} (km s ^{−1})		
GSC07380-01211	69	−6.99	−7.22	0.23	No
GSC07380-01363	...	−8.79	−8.61	0.18	No